and a fitting procedure described previously (Huang *et al*, 1991; Iida *et al*, 1993). Next, it was added to the extrapolated residual $H_2^{15}O$ TAC to obtain a TAC for $H_2^{15}O$ (A_w), and also subtracted from the second TAC to obtain a pure TAC for $^{15}O_2$ (A_o). For the $^{15}O_2$–$H_2^{15}O$ protocol, we first obtained the TAC for recirculating water during the first phase of $^{15}O_2$ administration as described above, and then separated the arterial TAC into pure TACs for $^{15}O_2$ (A_o) and for $H_2^{15}O$ (A_w) during the first phase. Second, we estimated the TAC for the residual radioactivity of $^{15}O_2$ during the second phase by extrapolating the estimated arterial $^{15}O_2$ TAC from the first phase as described above, and then obtained A_o and A_w. The preliminary validation of this procedure is described elsewhere (Kudomi *et al*, 2002).

The $C^{15}O$ sinogram data summed over 240 secs beginning at 120 secs after $C^{15}O$ inhalation, and reconstructed. The CBV images were then generated from the $C^{15}O$ images using the blood radioactivity concentration averaged over the scan period, with an assumption of a peripheral-to-central hematocrit ratio (R_{Hct}) of 0.85 (Phelps *et al*, 1979), a blood density of 1.06 g/mL, and a brain-tissue density of 1.04 g/mL (Lammertsma *et al*, 1987).

A set of CBF, OEF, and $CMRO_2$ images were calculated according to the DARG technique, using a set of integrated images ($\int_w Ci(t)dt$ and $\int_o Ci(t)dt$), a CBV image (V_B), and TACs for $H_2^{15}O$ (A_w) and $^{15}O_2$ (A_o) based on the formula described above, assuming $P = 0.8$ mL/g (Iida *et al*, 1991) and $Fv = 0.835$ (Mintun *et al*, 1984). Corresponding images were also calculated according to the three-step ARG using a procedure previously described (Shidahara *et al*, 2002). Briefly, the CBF image was calculated using the reconstructed image for $H_2^{15}O$, the initial part of the $H_2^{15}O$–$^{15}O_2$ scan (0 to 120 secs, $\int_w Ci(t)dt$), and the corresponding arterial TAC using a look-up-table procedure. Similarly, the OEF and $CMRO_2$ images were calculated using the $^{15}O_2$ part of the $^{15}O_2$–$H_2^{15}O$ scan (0 to 180 secs, $\int_o Ci(t)dt$), with corrections for recirculating water and the CBV compartment. Because $C^{15}O$ PET was performed only once for each animal, the resulting CBV image was used to calculate all DARG and three-step ARG images acquired during normocapnia and variable $PaCO_2$ conditions.

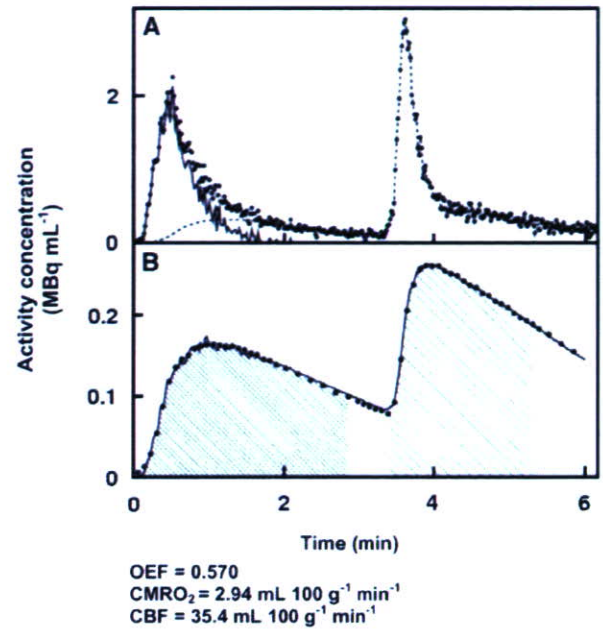

Figure 3 Example of blood and tissue TACs from DARG, in which administration of $^{15}O_2$ (2,200 MBq) was followed by $H_2^{15}O$ (370 MBq) with an interval of 3 mins during a 6-min PET scan. (**A**) Measured and estimated arterial TACs. Black dots, measured arterial TAC; solid line, estimated TAC of $^{15}O_2$ (A_o) generated by subtracting ^{15}O-labeled recirculating water from the observed value; broken line, estimated TAC of ^{15}O-labeled water (A_w) including recirculating and administered water (see data processing in Materials and methods). (**B**) Measured and predicted tissue TACs. Black dots, whole brain tissue TAC measured by PET. Solid line, predicted tissue TAC estimated from A_o and A_w with calculated functional values in a whole brain ROI. The area under each curve (shaded) corresponds to the PET data integrated after the administration of $^{15}O_2$ ($\int_o Ci(t)\,dt$) and then after $H_2^{15}O$ ($\int_w Ci(t)\,dt$) that was used for the calculation of functional values (see Theory section in Materials and methods). Calculated functional values in this ROI are listed below, and TACs are shown without decay correction. TAC, time activity curve; DARG, dual tracer autoradiographic method.

Table 1 Global values of CBF (gCBF), OEF (gOEF), and $CMRO_2$ ($gCMRO_2$) calculated by three-step ARG and DARG, and gOEF calculated by arterial-venous difference of oxygen contents

	Three-step ARG	*DARG*		*A–V*
		$H_2^{15}O$–$^{15}O_2$	$^{15}O_2$–$H_2^{15}O$	
gCBF (mL 100/g min)	30 ± 9	30 ± 9	32 ± 11	—
gOEF	0.51 ± 0.07	0.54 ± 0.04	0.56 ± 0.06	0.54 ± 0.06
$gCMRO_2$ (mL 100/g min)	2.7 ± 0.4	2.7 ± 0.2	2.9 ± 0.4	—

Three-step ARG, conventional three-step autoradiographic method; DARG, dual tracer autoradiographic method; A–V, arterial–inus blood sampling method. Values are presented as mean ± s.d. ($n = 6$).

Data Analysis

To assess the consistency of the calculated physiologic values, we obtained and analyzed the global and regional brain values separately. Magnetic resonance imaging images were de-skulled and coregistered to the CBF PET image by a rigid body transformation using statistic parametric mapping software (SPM 99, Wellcome Department of Neurology, London, UK). A region of interest (ROI) for the whole brain was drawn in every slice on the coregistered MRI images, using the GpetView (http://homepage2.nifty.com/peco/gpetview/gpetview.html) software, and transferred to all PET images obtained by three-step ARG and DARG ($H_2^{15}O$–$^{15}O_2$ and $^{15}O_2$–$H_2^{15}O$) to determine gCBF, gOEF, and $gCMRO_2$. We compared each variable between DARG and three-step ARG, and the gOEF value was compared with that of $gOEF_{A-V}$; all data are presented as means ± s.d. The paired *t*-test was applied to evaluate differences between methods, and $P<0.05$ was considered statistically significant. We plotted gOEF from DARG and $gOEF_{A-V}$ acquired during varied $PaCO_2$ against each other and performed regression analysis.

Regional values for CBF and $CMRO_2$ were obtained in 24 circular ROIs of 5-mm in diameter: two in frontal,

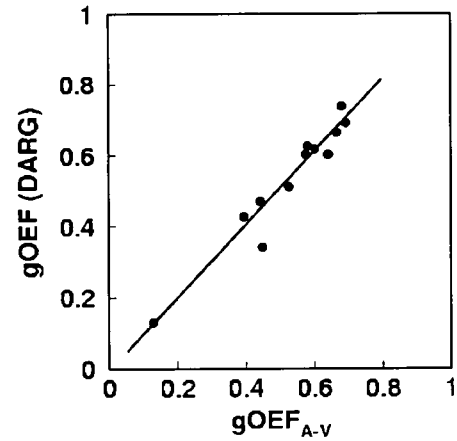

Figure 4 Plots of OEF measured by the arterio-sinus difference (gOEFA-V) and DARG (gOEF-DARG). The regression analysis exhibited a significant positive correlation with a slope close to unity ($r=0.963$, $P<0.001$, n (the number of observations) = 12). DARG was performed with an administration order of ^{15}O–$H_2^{15}O$. DARG, dual tracer autoradiographic method; OEF, oxygen extraction fraction.

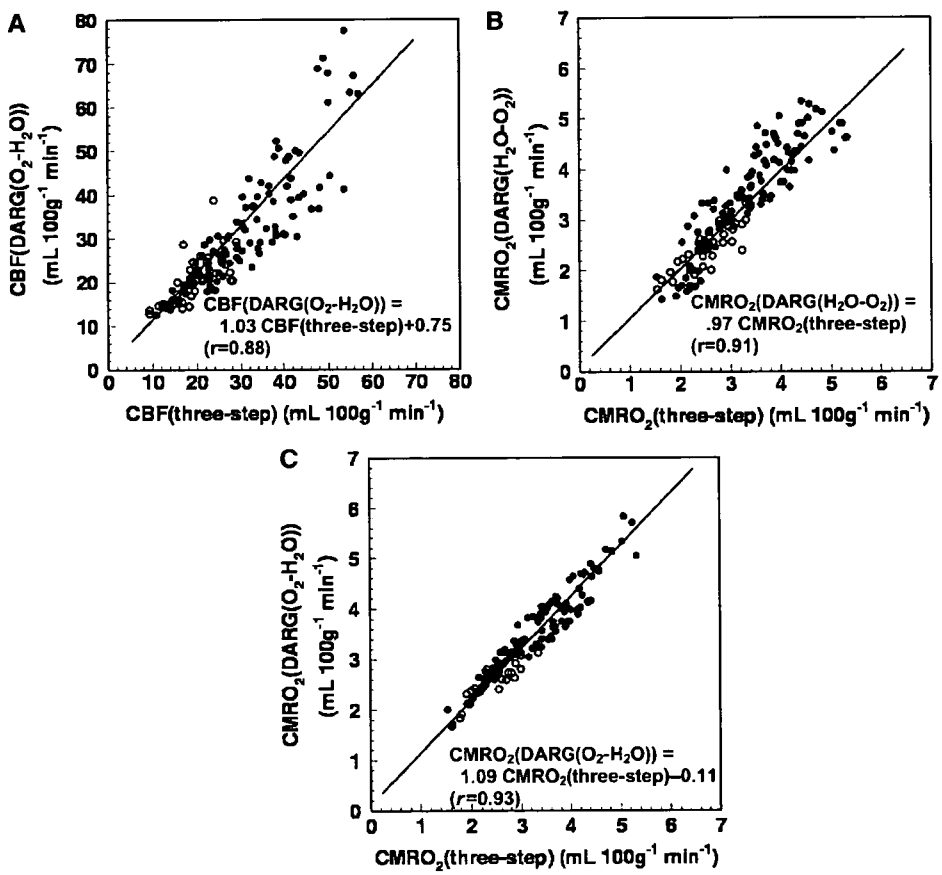

Figure 5 Relationships of the regional ROI values of (**A**) CBF by three-step ARG and by DARG($^{15}O_2$–$H_2^{15}O$), (**B**) $CMRO_2$ by three-step ARG and by DARG ($H_2^{15}O$–$^{15}O_2$), and (**C**) $CMRO_2$ by three-step ARG and by DARG ($^{15}O_2$–$H_2^{15}O$). The solid lines and equations in each figure show the regression line. ●, cortical region; ○, subcortical region.

Table 2 Regional values in DARG and NLF

Dataset Region of interest	*CBF(mL 100/g min)*		*OEF*		*$CMRO_2$ (mL 100/g min)*		p *(mL/g)*
	DARG	*NLF*	*DARG*	*NLF*	*DARG*	*NLF*	*NLF*
$H_2{}^{15}O$–$^{15}O_2$							
Frontal Cx.	27±6	29±6	0.51±0.10	0.58±0.09	2.5±0.6	2.5±0.6	0.81±0.11
Temporal Cx.	42±15	40±9	0.56±0.10	0.58±0.07	3.0±0.8	2.8±0.8	0.71±0.11
Parietal Cx.	39±13	32±10	0.51±0.10	0.57±0.15	2.6±0.9	2.4±0.9	0.83±0.08
Occipital Cx.	37±11	40±15	0.46±0.10	0.56±0.07	3.5±1.6	2.9±0.9	0.76±0.11
Sub-Cx	23±6	27±8	0.60±0.10	0.59±0.06	2.0±0.4	2.0±0.8	0.69±0.17
$^{15}O_2$–$H_2{}^{15}O$							
Frontal Cx.	30±6	30±6	0.57±0.10	0.60±0.09	3.1±0.4	3.2±0.3	0.72±0.14
Temporal Cx.	42±15	37±11	0.58±0.10	0.56±0.09	3.4±1.7	2.9±0.2	0.90±0.11
Parietal Cx.	41±16	36±10	0.60±0.10	0.61±0.09	3.4±0.8	3.3±0.4	0.90±0.15
Occipital Cx.	33±14	31±9	0.58±0.10	0.57±0.09	2.7±0.3	2.7±0.8	0.76±0.18
Sub-Cx	26±7	27±6	0.61±0.10	0.63±0.09	2.6±0.3	2.4±0.56	0.70±0.11

NLF, nonlinear fitting method; DARG, dual ARG method; Cx., cortex; *p*, partition coefficient.
For both $H_2{}^{15}O$–$^{15}O_2$ and $^{15}O_2$–$H_2{}^{15}O$ data sets, CBF, OEF, and $CMRO_2$ values for each region did not differ between NLF and DARG (Paired *t*-test, $P>0.05$).
Values are presented as mean±s.d. ($n=6$).

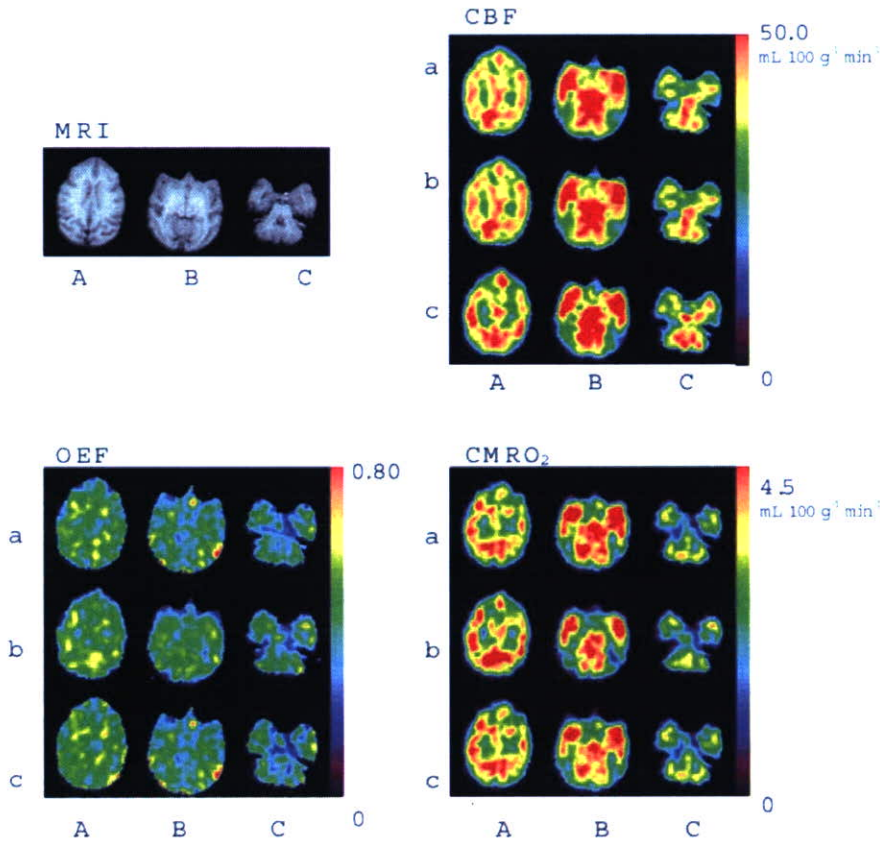

Figure 6 Functional images from one monkey obtained by (a) three-step ARG, (b) DARG $H_2^{15}O$–$^{15}O_2$, and (**C**) DARG $^{15}O_2$–$H_2^{15}O$. Images were axially sectioned at the level of the (A) lateral ventricle, (B) thalamus, and (C) cerebellum. Coregistered T_1-weighted MRI images are also presented at the upper left.

three in temporal, two in parietal, two in occipital cortical regions, and three in subcortical regions; data were recorded for each hemisphere. Although a great attention has been made in selecting small ROIs, the partial volume effect may not be minimized attributed to the small size of the brain in monkeys (approximately

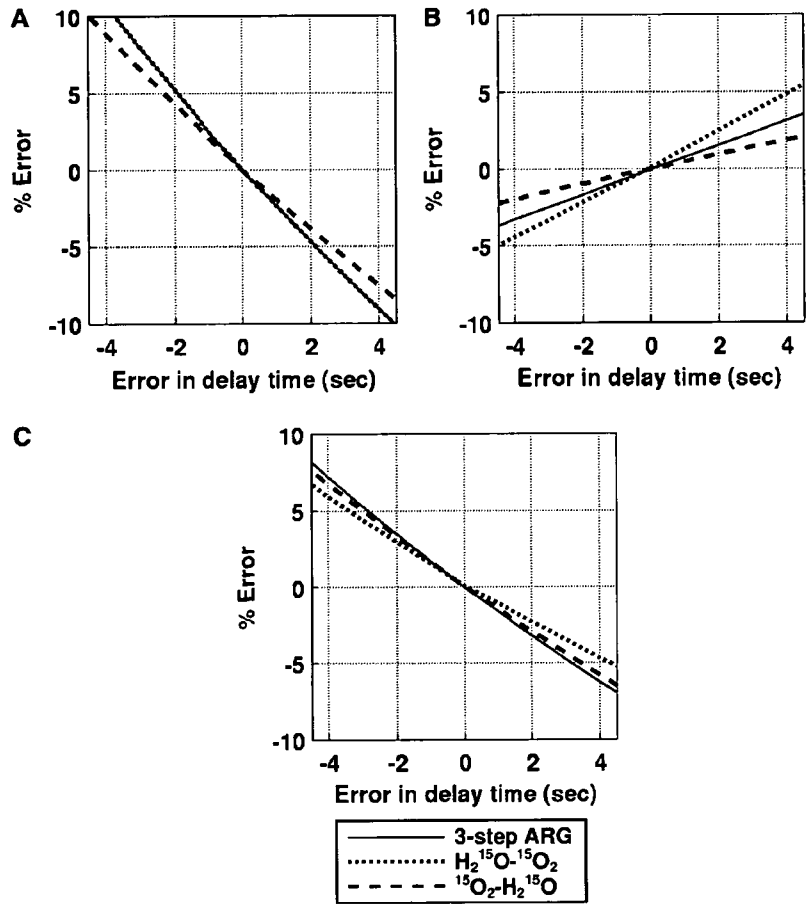

Figure 7 Error propagation from the error in input delay time to the functional parameters: (**A**) CBF, (**B**) OEF, and (**C**) $CMRO_2$. Positive and negative values of error in delay time indicate over- and undercorrection of delay time, respectively, whereas zero (secs) in the transverse axis corresponds to when the delay of measured artery input was accurately corrected to the true cerebral arterial input. Three-step ARG, conventional three-step autoradiographic method; $H_2^{15}O$–$^{15}O_2$, DARG with $H_2^{15}O$ followed by $^{15}O_2$; $^{15}O_2$–$H_2^{15}O$, DARG with $^{15}O_2$ followed by $H_2^{15}O$; DARG, dual tracer autoradiographic method.

50 mm in size). Regression analysis was performed comparing the values of CBF and $CMRO_2$ between three-step ARG and either DARG sequence. To test the validity of using a fixed p in the DARG protocol, regional CBF, OEF, and $CMRO_2$ values were also calculated using the NLF technique. Using a Gaussian–Newton algorithm, three parameters of f, E, and p were fitted to equation (2) using arterial input functions for H_2O and O_2, as determined previously. The CBV was fixed at each ROI using the $C^{15}O$ scan value, and all other parameters were fixed at the same values as described above. Tissue TACs for each region were extracted by averaging four TACs in frontal regions, six in temporal regions, four in parietal regions, four in occipital cortical regions, and six in subcortical ROI; those ROIs were projected to the dynamic PET images for H_2O–O_2 and O_2H_2O. In each region, CBF, OEF, and $CMRO_2$ values were computed by NLF and DARG and compared using a paired t-test. All data are presented as means ± s.d., and $P<0.05$ was considered statistically significant.

Error Analyses in Simulation

Error propagation was analyzed for four factors: delay and dispersion in arterial TAC, blood/tissue partition coefficient (P), and cerebral blood volume (V_B). It is known that the measured arterial TAC is delayed and more dispersed relative to the true input TAC in the brain because of the time it takes for blood to traverse the peripheral artery and catheter tube before reaching the detector (Iida *et al*, 1986, 1988, 1989, 2000; Lammertsma *et al*, 1990). Calculation of CBF using ARG PET always uses a fixed partition coefficient throughout the whole brain (ranging 0.8 to 0.9 mL/g) and does not evaluate it regionally (Herscovitch and Raichle, 1985; Iida *et al*, 1989, 1991; Shidahara *et al*, 2002). An error in CBV measured by the PET scan may also introduce errors in calculating the cerebral oxygen consumption (Mintun *et al*, 1984; Lammertsma *et al*, 1987).

Typical arterial input functions for water (A_w) and oxygen (A_o) were obtained from one monkey in this study and used after simulation as the true arterial TACs. Using these arterial TACs and equation (2), tissue TACs for water

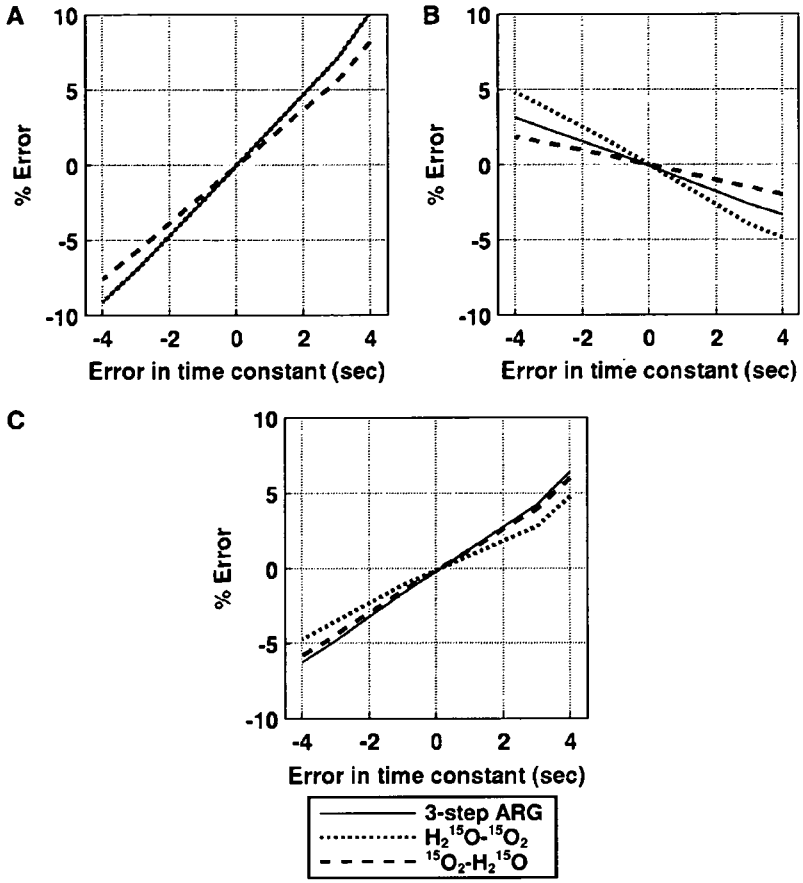

Figure 8 Error propagation from the error in the dispersion time constant to the functional parameters: (**A**) CBF, (**B**) OEF, and (**C**) $CMRO_2$. Positive and negative values of error in the dispersion time constant indicate over- and undercorrection, respectively, of dispersion time, whereas zero (secs) in the transverse axis corresponds to when the dispersion was accurately corrected to the tme cerebral arterial input. Three-step ARG, conventional three-step autoradiographic method; $H2^{15}O$–$^{15}O_2$, DARG with $H2^{15}O$ followed by $^{15}O_2$; $^{15}O_2$–$H_2^{15}O$, DARG with $^{15}O_2$ followed by $H_2^{15}O$; DARG, dual tracer autoradiographic method.

and oxygen were created using known values for normal brain tissue (CBF = 50 mL 100/g min, OEF = 0.4, CBV = 0.04 mL/g, P = 0.8 mL/g, Fv = 0.835, and R_{Hct} = 0.85). These TACs were used as true tissue TACs for three-step ARG. True tissue TACs for DARG were created by adding two tissue TACs for each tracer with a time lag of 3 mins, simulating the interval of administration. To simulate the error propagation resulting from errors in estimated delay time and dispersion time constants, the error in delay time or dispersion time was varied from −4 to 4 secs, where a positive error represents an overcorrection of delay time or dispersion time constant, and a negative error represents undercorrection, as described previously (Iida *et al*, 2000). Values for CBF, OEF, and $CMRO_2$ were calculated based on three-step ARG and DARG. To shift the dispersion time constants, the true arterial TAC was convoluted or deconvoluted with a simple exponential (Iida *et al*, 1986; Kanno *et al*, 1987). For simulating the error in the values of p and V_B, the value of p was varied from 0.7 to 0.9 mL/g, and that of V_B from 0.02 to 0.06 mL/g; in each situation, tissue TACs were created and CBF, OEF, and $CMRO_2$ values were calculated using these TACs, assuming P = 0.8 mL/g and V_B = 0.04 mL/g. Errors in these calculated values are presented as percentage differences from the normal values for each DARG and three-step ARG. In DARG, both orders of tracer administration were simulated.

Results

Animal Experiments

Figure 3 shows an example of measured and estimated blood TACs (A_o and A_w) and whole brain TAC in one $^{15}O_2$–$H_2^{15}O$ DARG PET experiment. In this experiment, $^{15}O_2$ (2,200 MBq) and $H_2^{15}O$ (370 MBq) were sequentially administrated in that order. As shown in this figure, the present method for extracting A_w and A_o TACs from measurements of arterial blood TAC accurately predicted the time course of the whole brain TAC.

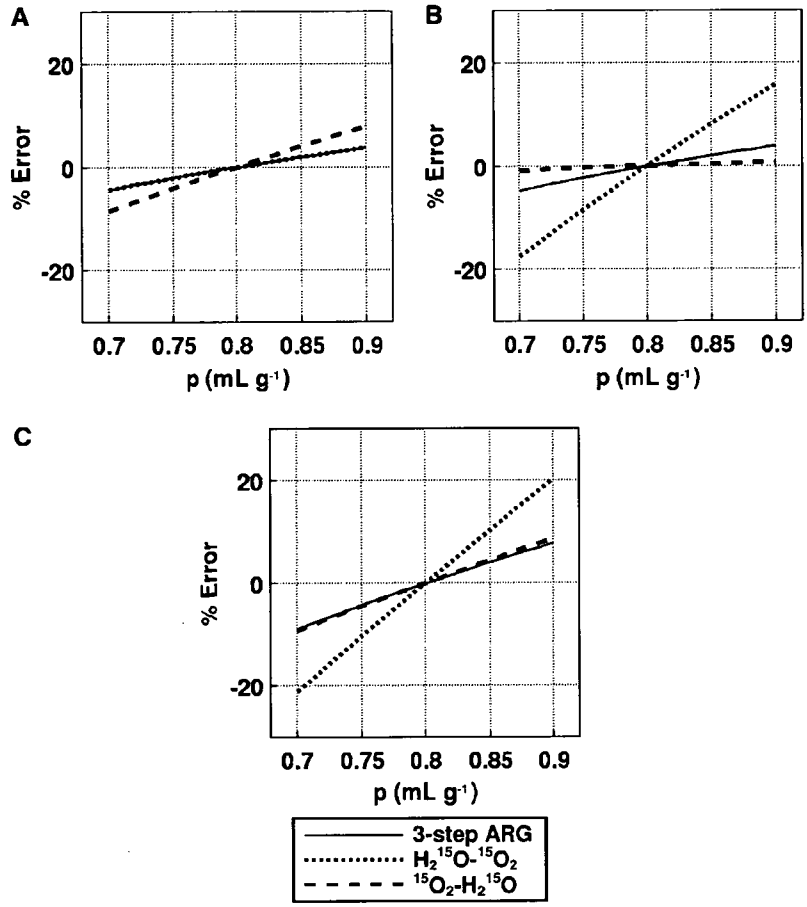

Figure 9 Error propagation from the partition coefficient to the functional parameters: (**A**) CBF, (**B**) OEF, and (**C**) $CMRO_2$. When the true p (transverse line) changed from 0.7 to 0.9 mL g^{-1}, the size of the error in each variable calculated, assuming $p = 0.8$ mL g^{-1}, was simulated. Three-step ARG, conventional three-step autoradiographic method; $H_2^{15}O$–$^{15}O_2$, DARG with $H_2^{15}O$ followed by $^{15}O_2$; $^{15}O_2$–$H_2^{15}O$, DARG with $^{15}O_2$ followed by $H_2^{15}O$; DARG, dual tracer autoradiographic method.

In Table 1, quantitative values of gCBF, $gCMRO_2$, and gOEF for whole brain are summarized. The paired t-test did not show any significant differences in any variable between three-step ARG and either DARG sequence order ($H_2^{15}O$–$^{15}O_2$ or $^{15}O_2$–$H_2^{15}O$) ($P > 0.05$, $n = 6$). Also, there were no significant differences in gOEF between either of the PET methods or the A–V method ($P > 0.05$, $n = 6$). For the measurements obtained during normocapnia, the $PaCO_2$, P_aO_2, S_aO_2, and hemoglobin values were 38.9 ± 1.4 mm Hg, 119 ± 12 mm Hg, $97.3\% \pm 1.2\%$, and 13.6 ± 1.0 g/dL, respectively; all of these are considered within the normal range.

Figure 4 shows the DARG-derived gOEF values plotted against $gOEF_{A-V}$ values, all obtained during $PaCO_2$ variation. The best-fit regression line can be expressed as $gOEF = 1.03 gOEF_{A-V} - 0.01$ ($r = 0.963$, $P < 0.001$, $n = 12$). The intercept is not significantly different from zero ($P > 0.05$), and the slope of the line is close to unity. During these measurements, $PaCO_2$ values ranged from 28 to 57 mm Hg.

The relationships of the regional ROI values between three-step ARG and DARG ($H_2^{15}O$–$^{15}O_2$ and $^{15}O_2$–$H_2^{15}O$) are shown in Figure 5. The obtained regression lines for CBF were CBF (DARG (H_2O–O_2)) = CBF (three-step) + 0.00 mL 100/g/min ($r = 1$) and CBF (DARG (O_2–H_2O)) = 1.03 CBF (three-step) + 0.75 mL 100/g/min ($r = 0.88$). For $CMRO_2$, the regression lines were $CMRO_2$ (DARG (H_2O–O_2)) = 0.97 $CMRO_2$ (three-step) + 0.00 mL 100/g/min ($r = 0.91$) and $CMRO_2$ (DARG (O_2–H_2O)) = 1.09 $CMRO_2$ (three-step) − 0.11 mL 100/g/min ($r = 0.93$), and showed that the values of slope were not significantly different from the unity.

In Table 2, values of CBF, OEF, and $CMRO_2$ in regional ROI computed by DARG and NLF are listed for each data set for both $^{15}O_2$–$H_2^{15}O$ and $H_2^{15}O$–$^{15}O_2$. In every region, for both data sets, the obtained CBF, OEF, and $CMRO_2$ values did not differ significantly between NLF and DARG (paired t-test, $P > 0.05$). In each region, the estimated value of p for NLF was not different from the assumed value of 0.8 (one

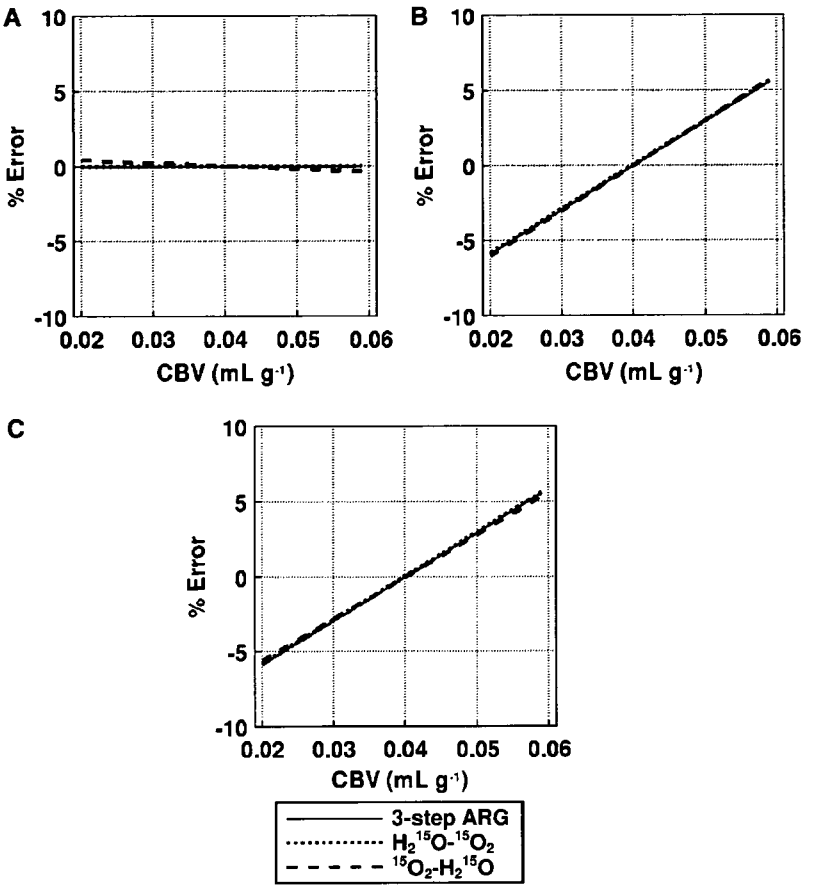

Figure 10 Error propagation from CBV to the functional parameters: (**A**) CBF, (**B**) OEF, and (**C**) $CMRO_2$. When the true CBV (transverse line) changed from 0.02 to 0.06 mL g^{-1}, the size of the error in each variable calculated, assuming CBV = 0.04 mL g^{-1}, was simulated. Three-step ARG, conventional three-step autoradiographic method; $H_2^{15}O$–$^{15}O_2$, DARG with $H_2^{15}O$ followed by $^{15}O_2$; $^{15}O_2$–$H_2^{15}O$, DARG with $^{15}O_2$ followed by $H_2^{15}O$; DARG, dual tracer autoradiographic method.

sample *t*-test, $P > 0.05$); however, two-way analysis of variance with 'region' and 'subject' as factors showed a statistically significant effect of 'region' on p ($F_{4,30} = 5.27$, $P = 0.029$). Its mean was the smallest in the subcortex (0.69 to 0.70 mL/g). Considering that subcortical ROI size involves not only white matter but also subcortical gray matter and ventricles, this result supports a previous notion that tissue mixtures cause an underestimation of p (Iida *et al*, 1989). Therefore, these results suggest that using a fixed p value seems not to cause significant bias in CBF, OEF, and $CMRO_2$.

Figure 6 provides a representative set of CBF, OEF, and $CMRO_2$ images generated by DARG and three-step ARG. The functional images generated from DARG were of comparable quality to those obtained using three-step ARG.

Error Analysis

Effects of delay correction errors: (Figure 7): For CBF, the error sensitivity of the DARG-$H_2^{15}O$–$^{15}O_2$ protocol was the same as that in three-step ARG, whereas the error sensitivity of the DARG-$^{15}O_2$–$H_2^{15}O$ protocol was smaller by 20%. For OEF, the error sensitivity in DARG-$H_2^{15}O$–$^{15}O_2$ was increased two-fold, while that in DARG-$^{15}O_2$–$H_2^{15}O$ was suppressed by 50%. For $CMRO_2$, the error sensitivity in DARG-$H_2^{15}O$–$^{15}O_2$ was suppressed by 40%, whereas that in $^{15}O_2$–$H_2^{15}O$ was almost equal to the value for three-step ARG. For example, when the error in the measured delay was 2 secs, errors in DARG were at most 5%, 3%, and 3% in CBF, OEF, and $CMRO_2$, respectively. Considering that the error estimation of delay would be up to 2 secs in the present procedure (Kanno *et al*, 1987; Shidahara *et al*, 2002), these results indicate that the error sensitivity to delay associated with DARG did not greatly exceed that from three-step ARG.

Effects of dispersion correction errors (Figure 8): For CBF, the error sensitivity in DARG $H_2^{15}O$–$^{15}O_2$ was similar to that associated with three-step ARG; in contrast, that in $^{15}O_2$–$H_2^{15}O$ was suppressed by 20%.

For OEF, the error sensitivity in $H_2^{15}O$–$^{15}O_2$ was increased two-fold, while that in $^{15}O_2$–$H_2^{15}O$ was decreased by 50%. For $CMRO_2$, the error sensitivity in DARG $H_2^{15}O$–$^{15}O_2$ was suppressed by 20%, but that in $^{15}O_2$–$H_2^{15}O$ was nearly equal to that of three-step ARG. The magnitude of errors introduced in CBF, OEF, and $CMRO_2$ were less than 5% for all estimation procedures even if there was 2 secs of error in estimating the time constant of dispersion (Iida *et al*, 1986). These results also indicate that the error sensitivity to dispersion in DARG does not significantly exceed that associated with three-step ARG.

Effects of the partition coefficient (Figure 9): For CBF, the error sensitivity in $H_2^{15}O$–$^{15}O_2$ was the same, and that in $^{15}O_2$–$H_2^{15}O$ was enhanced two-fold, as compared with three-step ARG. For OEF, the error sensitivity was enhanced three-fold in $H_2^{15}O$–$^{15}O_2$ relative to three-step ARG, and the magnitude of error was almost zero for $^{15}O_2$–$H_2^{15}O$. For $CMRO_2$, the error sensitivity was increased two-fold in $H_2^{15}O$–$^{15}O_2$ and was the same in $^{15}O_2$–$H_2^{15}O$, as compared with three-step ARG. Assuming that the variation in p is 5%, the magnitude of error in the CBF estimated in $^{15}O_2$–$H_2^{15}O$ was at most 3.5%, whereas the error in OEF and $CMRO_2$ in $H_2^{15}O$–$^{15}O_2$ was 7%. Although the error sensitivities in $H_2^{15}O$–$^{15}O_2$ for OEF and $CMRO_2$ were somewhat larger than those associated with three-step ARG, the overall error sensitivity in DARG was similar to that in three-step ARG.

Effects of blood volume (Figure 10): The error sensitivities in both DARG experiments were identical to those obtained from three-step ARG. The magnitude of error introduced into the CBF estimate were less than 1%, and that for OEF and $CMRO_2$ was less than 5% in all methods, even assuming a true CBV of 0.06 mL/g.

This simulation study shows that the error sensitivity introduced in the quantitative values of CBF, OEF, and $CMRO_2$ for the first phase of the dynamic PET scan used in DARG was nearly the same as that in three-step ARG. In contrast, the error for the second phase was either enhanced or suppressed, depending on the relationship of the error between measured or assumed parameters and the estimate of residual radioactivity.

Finally, we have estimated the sensitivity in diseased tissue that simulates decreased CBF with elevated OEF ($f=20$ mL 100/g min and $E=0.7$), namely the ischemic lesion. The magnitude of error in the functional values of this tissue was roughly the same in terms of delay and dispersion, and was relatively smaller in terms of p and CBV, than the magnitude of error for assumed normal tissue. For example, when assumed 5% error in P, the magnitude of error introduced in CBF, OEF and $CMRO_2$ in the $H_2^{15}O$–$^{15}O_2$ scan was 1.5%, 2%, and 2% respectively, whereas that in $H_2^{15}O$–$^{15}O_2$ was 3%, 0%, and 3%, respectively.

Discussion

In this study, we have proposed a novel, rapid PET technique for quantitative assessment of both CBF and $CMRO_2$ from a single PET scanning with sequential administration of two tracers. This article described the validity of this technique in anesthetized monkeys at rest and during varied $PaCO_2$ conditions. There was no significant difference in CBF, OEF, or $CMRO_2$ values at rest, as compared with those obtained using three-step ARG. The estimated OEF values were also found to be in a good agreement with those derived from arterio-sinus blood sampling for a wide physiologic range. The image quality generated by DARG was identical to that of three-step ARG. The simulation also showed that the errors in the estimated parameters attributed to errors in delay, dispersion and the assumed partition coefficient was in the same level as compared with that of the three-step ARG. It should also be noted that the error sensitivity to the CBV was reasonably small, namely almost no errors in CBF, and only $\pm 5\%$ errors in OEF and $CMRO_2$ are caused even if $\pm 50\%$ errors are included in CBV. These findings suggest that the DARG technique provides CBF and $CMRO_2$ images with reasonable accuracy and quality, and also allows multiple assessment of CBF/$CMRO_2$, provided that a single CBV scan is performed.

The DARG technique provides multiple parameter mapping of CBF and $CMRO_2$ from a single PET scan during sequential administration of two tracers of $H_2^{15}O$ and $^{15}O_2$ (or $^{15}O_2$ and $H_2^{15}O$). Multiple tracer approach has been applied to ^{11}C-labeled tracers for mapping multiple receptor ligands (Koeppe *et al*, 2001). Another application of this approach is the repeat assessment of CBF. Watabe *et al* (2002) showed that CBF images can be quantitated at much shorter interval than the previous protocol, typically at 90 secs, from sequential PET scanning during repeat $H_2^{15}O$ administration at 90 secs interval

The measured OEF, CBF, and $CMRO_2$ values obtained in this study were consistent with previous studies. OEF values in this study were 0.51 ± 0.07 from three-step ARG, 0.54 ± 0.04 from DARG ($H_2^{15}O$–$^{15}O_2$), 0.56 ± 0.06 from DARG ($^{15}O_2$–$H_2^{15}O$), and 0.54 ± 0.06 from arterio-sinus blood sampling. In anesthetized monkeys, Altman *et al* (1991) obtained OEF values of 0.53 ± 0.13 from arterio-sinus blood sampling. Using steady-state PET, others have measured OEFs ranging from 0.42 to 0.58 in normal tissues of anesthetized monkeys (Altman *et al*, 1991; Pappata *et al*, 1993; Touzani *et al*, 1995; Young *et al*, 1996; Schumann *et al*, 1996; Frykholm *et al*, 2000). Moreover, the values of gCBF in the present PET study were 30 ± 9 mL 100/g min from three-step ARG, 30 ± 9 mL 100/g min from

DARG ($H_2^{15}O$–$^{15}O_2$), and 32 ± 11 mL 100/g min from DARG ($^{15}O_2$–$H_2^{15}O$), and the $CMRO_2$ values were 2.7 ± 0.4 from three-step ARG, 2.7 ± 0.2 mL 100/g min from DARG ($H_2^{15}O$–$^{15}O_2$), and 2.9 ± 0.4 mL 100/g min from DARG ($^{15}O_2$–$H_2^{15}O$). Previously reported values varied from 27 to 37 mL 100/g min for CBF and 2.4 to 3.4 mL 100/g min for $CMRO_2$ (Altman *et al*, 1991; Pappata *et al*, 1993; Touzani *et al*, 1995; Young *et al*, 1996; Schumann *et al*, 1996; Frykholm *et al*, 2000). Variations are because of the differences in monkey species, physiologic conditions, anesthetic agent used, PET scanner, and methodology; the current results clearly show that the DARG method can be used to determine these physiologic parameters with a high degree of accuracy.

There has not been systematic error sensitivity analysis for the conventional three-step ARG method. We thus have performed a simulation study to evaluate the error sensitivity for both the three-step ARG and DARG techniques. The error sensitivity appeared to be almost identical for all error sources estimated in the simulation. Small differences were, however, seen in particular cases obtained in this experiment. These differences may have arisen because of incorrect estimation of residual radioactivity in the second phase of the PET data. For example, when the true p is larger than the value assumed for $H_2^{15}O$–$^{15}O_2$, the CBF will be estimated as larger than the true value. Thus, washout of water will be overestimated, leading to a lower estimate of residual radioactivity. Underestimation of the residual radioactivity and large p values results in an overestimation of oxygen uptake (OEF), thus increasing the error in the $CMRO_2$ value. It is also notable that when the delay was overcorrected in $H_2^{15}O$–$^{15}O_2$, the error in $CMRO_2$ decreases compared with three-step ARG. The CBF becomes smaller than the true value and the amount of residual radioactivity will also be estimated to be smaller, causing overestimation of oxygen uptake (OEF). As a result, similar magnitudes of overestimation of OEF and underestimation of CBF will cancel the error in $CMRO_2$.

The present model provides pixel-by-pixel estimates of CBF, $CMRO_2$, and OEF based on data from a single PET scan, assuming a constant partition coefficient (p) for $H_2^{15}O$, as has been perfprmed for $H_2^{15}O$ autoradiography (Herscovitch *et al*, 1983; Raichle *et al*, 1983) and the three-step method (Mintun *et al*, 1984). The error in p propagates not only to CBF but also to OEF and $CMRO_2$. We used a fixed value of 0.8 mL/g for p, which was empirically determined so as to minimize the tissue mixture associated with the limited spatial resolution of PET scanner (Iida *et al*, 1989, 1991). The simulation study showed that the range of errors was almost within an acceptable range. Regional analysis also showed that the CBF, OEF, and $CMRO_2$ values provided by DARG were consistent with by NLF in normal monkeys. Thus, using a fixed p value in DARG should not cause significant bias provided that CBF, OEF, and $CMRO_2$ are of interest. However, this should be further validated in humans, as the effective p value could be affected by the tissue mixture and the magnitude of this effect might be different in human (Iida *et al*, 1991).

Several previous studies showed the feasibility of fixing a p value for $H_2^{15}O$ ARG (Herscovitch and Raichle, 1985; Kanno *et al*, 1987; Iida *et al*, 1989) and the three-step ARG (Mintun *et al*, 1984; Iida *et al*, 1993). One may argue the adequacy of this assumption in diseased tissues, that is, the p values may be increased in edematous regions, or decreased in the area of necrotic tissue. In case CBF is reduced in such lesions, errors in the estimated parameters would be small, because a linear relationship is expected between the tissue-radioactivity counts and the physiologic parameters, and the p does not contribute significantly to the kinetic behavior of the tracer accumulation. However, a great error can be expected if CBF is at a high range in the area of reduced p, as only a small change in p may cause large changes in the tissue accumulation of the tracers. Exact magnitude is unknown, and should be evaluated carefully for each of diseased conditions.

The present method has several advantages over three-step ARG. It eliminates the time required for radioactive decay between the $H_2^{15}O$ and $^{15}O_2$ scans, thus shortening the procedure by at least 10 mins compared with the three-step method. Importantly, it also minimizes the error resulting from physiologic fluctuations. Kinetic models of CBF-$CMRO_2$ used in PET techniques assume constant physiologic conditions throughout all PET scans, and $CMRO_2$ is mathematically dependent on CBF. Thus, physiologic changes during PET measurement may underlie in part the errors in quantitative values. It is well known that CBF easily varies with $PaCO_2$ (Grubb *et al*, 1974) and PaO_2 (Borgstrom *et al*, 1975; Johannsson and Siesjo, 1975); however, $CMRO_2$ remains constant. In fact, Hattori *et al* (2004) recently showed that OEF values in three-step method were not identical to those in $gOEF_{A-V}$ in human, suggesting the presence of physiologic change during the measurement. The present method may also make physiologic interpretations of flow and metabolism more accurate (Hayashi *et al*, 2003). Finally, it allows evaluation of coupling or uncoupling of CBF and $CMRO_2$ during functional activation or pharmacological stress, such as that induced by acetazolamide used for assessment of cerebral vascular reserves.

Ohta *et al* (1992) showed another technique for the rapid estimation of CBF, OEF, and $CMRO_2$ from a 3-min single PET scan following bolus inhalation of $^{15}O_2$. This approach does not take into account recirculating water and involves a mathematical formula with weighted integration to calculate these quantitative values. However, the generated functional images suffer from statistical noise, which is attributed to the need for determination of multiple

parameters from a small amount of time-varying data. Cerebral blood flow images, in particular, suffer significantly from noise; precise determination of CBF often requires another PET scan with $H_2^{15}O$ injection (Meyer *et al*, 1987; Ohta *et al*, 1999; Fujita *et al*, 1999; Mintun *et al*, 2002). In contrast, the present approach can generate images of reasonable quality from a single 6-min PET scan. Although currently it still requires another $C^{15}O$ scan for CBV correction, we believe that an additional mathematical formulation strategy, such as the basis function method (Gunn *et al*, 1997) could eliminate this need. In addition, to shorten the time for the transmission scan, we could possibly apply a segmented attenuation correction technique (Xu *et al*, 1994, 1996). We believe that the total PET scan time for measuring CBF and $CMRO_2$, for which patients need to be on the bed of the PET scanner, could be minimized to around 10 mins.

In the present study, the recirculating water in the arterial blood has been measured directly and continuously from separated plasma. This is laborious and may limit the use of this protocol for clinical studies. However, Iida *et al* (1993) have estimated the amount of recirculating water and showed that its amount can be predicted using a single compartment model in three-step ARG in normal human subjects. This method eliminates the need for plasma separation and simplifies the PET procedure (Hatazawa *et al*, 1995; Shidahara *et al*, 2002). However, as this method depends on inter-subject variation of the arterial $^{15}O_2$ TAC (which yields a bias in the $CMRO_2$ in DARG), its validity requires further evaluation in human studies.

Although the present study provided images of relatively good quality, image quality depends on many different factors, such as the interval, (relative) dose, and order of the two administered tracers. Given a shorter interval time between tracer administrations, a larger amount of residual radioactivity from the first tracer remains during the image acquisition for the second tracer, degrading the quality of the image calculated during the second phase of the procedure. We fixed the time interval to 3 mins in the present study based on preliminary simulations (Iida *et al*, 2002), which suggested that images of an equivalent quality to three-step ARG could be obtained if the time interval was at least 3 mins. The deteriorated image quality because of the second tracer can be compensated for if the amount of the second tracer is increased, so long as there are no mitigating factors such as scatter, random coincidence, and event loss because of dead time. The effects on image quality resulting from the alteration of dosage parameters are complex, and parameter changes may interact in ways that interfere with each other. From a practical point of view, the reliability of specific parameters may be limited by properties of each tracer that depend on the labelling efficiency of $H_2^{15}O$ synthesis, and can differ between supply facilities, as well as the distance and flow rate from the synthesizer to the PET scanner. Further studies are required to optimize these parameters to maximize image quality when applying this method to human studies.

In conclusion, although several issues remain to be investigated, this study shows the feasibility of rapid and simultaneous measurement of CBF and $CMRO_2$ using a single PET scan and the sequential administration of two tracers. Both experimental and simulation studies show that the DARG method provides reasonable accuracy for quantitative values of CBF, OEF, and $CMRO_2$, and that the quality of the images produced was comparable to that of three-step ARG. The present study suggests that this method may be applicable to the estimation of CBF and $CMRO_2$ in humans, particularly in acute to subacute ischemic patients or in the multiple assessment of CBF/$CMRO_2$ at different physiologic conditions.

Acknowledgements

The authors gratefully acknowledge Mr N Ejima for providing the operating cyclotron and daily maintenance of the CTI ECAT HR, and would also like to thank the staff of the Department of Investigative Radiology, Research Institute, National Cardiovascular Center.

References

Altman DI, Lich LL, Powers WJ (1991) Brief inhalation method to measure cerebral oxygen extraction fraction with PET: accuracy determination under pathologic conditions. *J Nucl Med* 32:1738–41

Borgstrom L, Johannsson H, Siesjo BK (1975) The relationship between arterial pO_2 and cerebral blood flow in hypoxic hypoxia. *Acta Physiol Scand* 93:423–32

Correia JA, Alpert NM, Buxton RB, Ackerman RH (1985) Analysis of some errors in the measurement of oxygen extraction and oxygen consumption by the equilibrium inhalation method. *J Cereb Blood Flow Metab* 5:591–9

Frackowiak RS, Jones T, Lenzi GL, Heather JD (1980*a*) Regional cerebral oxygen utilization and blood flow in normal man using oxygen-15 and positron emission tomography. *Acta Neurol Scand* 62:336–44

Frackowiak RS, Lenzi GL, Jones T, Heather JD (1980*b*) Quantitative measurement of regional cerebral blood flow and oxygen metabolism in man using ^{15}O and positron emission tomography: theory, procedure, and normal values. *J Comput Assist Tomogr* 4:727–36

Frykholm P, Andersson JL, Valtysson J, Silander HC, Hillered L, Persson L, Olsson Y, Yu WR, Westerberg G, Watanabe Y, Langstrom B, Enblad P (2000) A metabolic threshold of irreversible ischemia demonstrated by PET in a middle cerebral artery occlusion-reperfusion primate model. *Acta Neurol Scand* 102:18–26

Fujita H, Kuwabara H, Reutens DC, Gjedde A (1999) Oxygen consumption of cerebral cortex fails to increase during continued vibrotactile stimulation. *J Cereb Blood Flow Metab* 19:266–71

Grubb Jr RL, Raichle ME, Eichling JO, Ter-Pogossian MM (1974) The effects of changes in $PaCO_2$ on cerebral blood volume, blood flow, and vascular mean transit time. *Stroke* 5:630–9

Gunn RN, Lammertsma AA, Hume SP, Cunningham VJ (1997) Parametric imaging of ligand-receptor binding in PET using a simplified reference region model. *Neuroimage* 6:279–87

Hatazawa J, Fujita H, Kanno I, Satoh T, Iida H, Miura S, Murakami M, Okudera T, Inugami A, Ogawa T, Shimosegawa E, Noguchi K, Shoji Y, Kanno I (1995) Regional cerebral blood flow, blood volume, oxygen extraction fraction, and oxygen utilization rate in normal volunteers measured by the autoradiographic technique and the single breath inhalation method. *Ann Nucl Med* 9:15–21

Hattori N, Bergsneider M, Wu HM, Glenn TC, Vespa PM, Hovda DA, Phelps ME, Huang SC (2004) Accuracy of a method using short inhalation of ^{15}O–O_2 for measuring cerebral oxygen extraction fraction with PET in healthy humans. *J Nucl Med* 45:765–70

Hayashi T, Watabe H, Kudomi N, Kim KM, Enmi J, Hayashida K, Iida H (2003) A theoretical model of oxygen delivery and metabolism for physiologic interpretation of quantitative cerebral blood flow and metabolic rate of oxygen. *J Cereb Blood Flow Metab* 23:1314–23

Herscovitch P, Markham J, Raichle ME (1983) Brain blood flow measured with intravenous $H_2(15)O$. I. Theory and error analysis. *J Nucl Med* 24:782–9

Herscovitch P, Raichle ME (1985) What is the correct value for the brain–blood partition coefficient for water? *J Cereb Blood Flow Metab* 5:65–9

Ho D, Feng D (1999) Rapid algorithms for the construction of cerebral blood flow and oxygen utilization images with oxygen-15 and dynamic positron emission tomography. *Comput Methods Programs Biomed* 58:99–117

Holden JE, Eriksson L, Roland PE, Stone-Elander S, Widen L, Kesselberg M (1988) Direct comparison of single-scan autoradiographic with multiple-scan least-squares fitting approaches to PET $CMRO_2$ estimation. *J Cereb Blood Flow Metab* 8:671–80

Huang SC, Barrio JR, Yu DC, Chen B, Grafton S, Melega WP, Hoffman JM, Satyamurthy N, Mazziotta JC, Phelps ME. (1991) Modelling approach for separating blood time–activity curves in positron emission tomographic studies. *Phys Med Biol* 36:749–61

Huang SC, Feng DG, Phelps ME (1986) Model dependency and estimation reliability in measurement of cerebral oxygen utilization rate with oxygen-15 and dynamic positron emission tomography. *J Cereb Blood Flow Metab* 6:105–19

Iida H, Higano S, Tomura N, Shishido F, Kanno I, Miura S, Murakami M, Takahashi K, Sasaki H, Uemura K (1988) Evaluation of regional differences of tracer appearance time in cerebral tissues using [^{15}O] water and dynamic positron emission tomography. *J Cereb Blood Flow Metab* 8:285–8

Iida H, Kanno I, Miura S, Murakami M, Takahashi K, Uemura K (1986) Error analysis of a quantitative cerebral blood flow measurement using $H_2(15)O$ autoradiography and positron emission tomography, with respect to the dispersion of the input function. *J Cereb Blood Flow Metab* 6:536–45

Iida H, Kanno I, Miura S, Murakami M, Takahashi K, Uemura K (1989) A determination of the regional brain/blood partition coefficient of water using dynamic positron emission tomography. *J Cereb Blood Flow Metab* 9:874–85

Iida H, Jones T, Miura S (1993) Modeling approach to eliminate the need to separate arterial plasma in oxygen-15 inhalation positron emission tomography. *J Nucl Med* 34:1333–40

Iida H, Kanno I, Miura S (1991) Rapid measurement of cerebral blood flow with positron emission tomography. *Chiba Found Symp* 163:23–37; discussion 37–42

Iida H, Law I, Pakkenberg B, Krarup-Hansen A, Eberl S, Holm S, Hansen AK, Gundersen HJ, Thomsen C, Svarer C, Ring P, Friberg L, Paulson OB (2000) Quantitation of regional cerebral blood flow corrected for partial volume effect using O-15 water and PET: I. Theory, error analysis, and stereologic comparison. *J Cereb Blood Flow Metab* 20:1237–51

Iida H, Miyake Y, Hayashi T, Kudomi N, Ogawa M, Teramoto N, Kim KM, Oka H, Hayashida K (2002) A new strategy for rapid clinical imaging of $rCMRO_2$, rCBF and rOEF using PET. *J Nucl Med* 43(Suppl):62P

Johannsson H, Siesjo BK (1975) Cerebral blood flow and oxygen consumption in the rat in hypoxic hypoxia. *Acta Physiol Scand* 93:269–76

Kanno I, Iida H, Miura S, Murakami M, Takahashi K, Sasaki H, Inugami A, Shishido F, Uemura K (1987) A system for cerebral blood flow measurement using an $H_2^{15}O$ autoradiographic method and positron emission tomography. *J Cereb Blood Flow Metab* 7:143–53

Kety SS, Schmidt CF (1948) The nitrous oxide method for the quantitative determination of cerebral blood flow in man: theory, procedure and normal values. *J Clin Invest* 27:476–84

Koeppe RA, Raffel DM, Snyder SE, Ficaro EP, Kilbourn MR, Kuhl DE (2001) Dual-[^{11}C]tracer single-acquisition positron emission tomography studies. *J Cereb Blood Flow Metab* 21:1480–92

Kudomi N, Choi C, Watabe H, Kim KM, Shidahara M, Ogawa M, Teramoto N, Sakamoto E, Iida H (2003) Development of a GSO Detector Assembly for a Continuous Blood Sampling System. *IEEE Trans Nucl Sci* 50:70–3

Kudomi N, Watabe H, Kim KM, Hayashida K, Hayashi T, Iida H (2002) Estimation of input function for rapid dual table ARG method. *IEEE Nucl Sci Symp Conference Record* M7–223

Lammertsma AA, Baron JC, Jones T (1987) Correction for intravascular activity in the oxygen-15 steady-state technique is independent of the regional hematocrit. *J Cereb Blood Flow Metab* 7:372–4

Lammertsma AA, Cunningham VJ, Deiber MP, Heather JD, Bloomfield PM, Nutt J, Frackowiak RS, Jones T (1990) Combination of dynamic and integral methods for generating reproducible functional CBF images. *J Cereb Blood Flow Metab* 10:675–86

Lammertsma AA, Heather JD, Jones T, Frackowiak RS, Lenzi GL (1982) A statistical study of the steady state technique for measuring regional cerebral blood flow and oxygen utilisation using ^{15}O. *J Comput Assist Tomogr* 6:566–73

Lammertsma AA, Jones T (1983) Correction for the presence of intravascular oxygen-15 in the steady-state technique for measuring regional oxygen extraction ratio in the brain: 1. Description of the method. *J Cereb Blood Flow Metab* 3:416–24

Meyer E, Tyler JL, Thompson CJ, Redies C, Diksic M, Hakim AM (1987) Estimation of cerebral oxygen utilization rate by single-bolus $^{15}O_2$ inhalation and

dynamic positron emission tomography. *J Cereb Blood Flow Metab* 7:403–14

Mintun MA, Raichle ME, Martin WR, Herscovitch P (1984) Brain oxygen utilization measured with O-15 radiotracers and positron emission tomography. *J Nucl Med* 25:177–87

Mintun MA, Vlassenko AG, Shulman GL, Snyder AZ (2002) Time-related increase of oxygen utilization in continuously activated human visual cortex. *Neuroimage* 16:531–7

Ohta S, Meyer E, Thompson CJ, Gjedde A (1992) Oxygen consumption of the living human brain measured after a single inhalation of positron emitting oxygen. *J Cereb. Blood Flow Metab* 12:175–92

Ohta S, Reutens DC, Gjedde A (1999) Brief vibrotactile stimulation does not increase cortical oxygen consumption when measured by single inhalation of positron emitting oxygen. *J Cereb Blood Flow Metab* 19:260–5

Okazawa H, Yamauchi H, Sugimoto K, Takahashi M, Toyoda H, Kishibe Y, Shio H (2001a) Quantitative comparison of the bolus and steady-state methods for measurement of cerebral perfusion and oxygen metabolism: positron emission tomography study using ^{15}O-gas and water. *J Cereb Blood Flow Metab* 21:793–803

Okazawa H, Yamauchi H, Sugimoto K, Toyoda H, Kishibe Y, Takahashi M (2001b) Effects of acetazolamide on cerebral blood flow, blood volume, and oxygen metabolism: a positron emission tomography study with healthy volunteers. *J Cereb Blood Flow Metab* 21: 1472–9

Pappata S, Fiorelli M, Rommel T, Hartmann A, Dettmers C, Yamaguchi T, Chabriat H, Poline JB, Crouzel C, Di Giamberardino L, Baron JC (1993) PET study of changes in local brain hemodynamics and oxygen metabolism after unilateral middle cerebral artery occlusion in baboons. *J Cereb Blood Flow Metab* 13:416–24

Phelps ME, Huang SC, Hoffman EJ, Kuhl DE (1979) Validation of tomographic measurement of cerebral blood volume with C-11-labeled carboxyhemoglobin. *J Nucl Med* 20:328–34

Raichle ME, Martin WR, Herscovitch P, Mintun MA, Markham J (1983) Brain blood flow measured with intravenous $H_2^{15}O$. II. Implementation and validation. *J Nucl Med* 24:790–8

Sadato N, Yonekura Y, Senda M, Iwasaki Y, Matoba N, Tamaki N, Sasayama S, Magata Y, Konishi J. (1993) PET and the autoradiographic method with continuous inhalation of oxygen-15-gas: theoretical analysis and comparison with conventional steady-state methods. *J Nucl Med* 34:1672–80

Schumann P, Touzani O, Young AR, Verard L, Morello R, MacKenzie ET (1996) Effects of indomethacin on cerebral blood flow and oxygen metabolism: a positron emission tomographic investigation in the anesthetized baboon. *Neurosci Lett* 220:137–41

Shidahara M, Watabe H, Kim KM, Oka H, Sago M, Hayashi T, Miyake Y, Ishida Y, Hayashida K, Nakamura T, Iida H (2002) Evaluation of a commercial PET tomograph-based system for the quantitative assessment of rCBF, rOEF and $rCMRO_2$ by using sequential administration of ^{15}O-labeled compounds. *Ann Nucl Med* 16:317–27

Subramanyam R, Alpert NM, Hoop Jr B, Brownell GL, Taveras JM (1978) A model for regional cerebral oxygen distribution during continuous inhalation of $^{15}O_2$, $C^{15}O$, and $C^{15}O_2$. *J Nucl Med* 19:48–53

Touzani O, Young AR, Derlon JM, Beaudouin V, Marchal G, Rioux P, Mezenge F, Baron JC, MacKenzie ET (1995) Sequential studies of severely hypometabolic tissue volumes after permanent middle cerebral artery occlusion. A positron emission tomographic investigation in anesthetized baboons. *Stroke* 26:2112–9

Vafaee MS, Gjedde A (2000) Model of blood-brain transfer of oxygen explains nonlinear flow-metabolism coupling during stimulation of visual cortex. *J Cereb Blood Flow Metab* 20:747–54

Watabe H, Konodo Y, Kim KM, Shidahara M, Iida H (2002) Shortening rCBF Measurement Interval in $[^{15}O]H_2O$ PET. In: *Brain imaging using PET* (Senda M, Kimura Y, Herscovitch P, eds), San Diego: Academic Press, 195–200

Xu M, Cutler PD, Luk WK (1996) Adaptive segmented attenuation correction for whole-body PET imaging. *IEEE Trans Nucl Sci* 43:331–6

Xu M, Luk WK, Cutler PD, Digby WM (1994) Local threshold for segmented attenuation correction of pet imaging of the thorax. *IEEE Trans Nucl Sci* 41:1532–7

Young AR, Sette G, Touzani O, Rioux P, Derlon JM, MacKenzie ET, Baron JC (1996) Relationships between high oxygen extraction fraction in the acute stage and final infarction in reversible middle cerebral artery occlusion: an investigation in anesthetized baboons with positron emission tomography. *J Cereb Blood Flow Metab* 16:1176–88

Available online at www.sciencedirect.com
SCIENCE DIRECT
Neuroscience Research 52 (2005) 357–361
Neuroscience Research
www.elsevier.com/locate/neures

Understanding of cerebral energy metabolism by dynamic living brain slice imaging system with [^{18}F]FDG

Mikako Ogawa [a], Hiroshi Watabe [b], Noboru Teramoto [b], Yoshinori Miyake [b], Takuya Hayashi [b], Hidehiro Iida [b], Tetsuhito Murata [c], Yasuhiro Magata [a,*]

[a] *Photon Medical Research Center, Hamamatsu University School of Medicine, Laboratory of Genome Bio-Photonics, 1-20-1 Handayama, Hamamatsu 431-3192, Japan*
[b] *Department of Investigative Radiology, Research Institute, National Cardiovascular Center, Osaka, Japan*
[c] *Department of Neuropsychiatry and Biomedical Imaging Research Center, Faculty of Medical Sciences, University of Fukui, Fukui, Japan*

Received 1 February 2005; accepted 18 April 2005
Available online 17 May 2005

Abstract

Recently, lactate has been receiving great attention as an energy substrate in the brain. In this study, the role of lactate was evaluated by "bioradiography" system with 2-deoxy-2-[^{18}F]fluoro-D-glucose ([^{18}F]FDG), which is a positron emitting radiotracer for glucose uptake quantification. "Bioradiography" is the dynamic living tissue slice imaging system for positron-emitter labeled compounds. We investigated the brain energy metabolism under resting state and neural activated conditions induced by KCl addition. The monocarboxylate transporter inhibitor, α-cyano-4-hydroxycinnamate (4-CIN), had no effect on [^{18}F]FDG uptake rate in rat brain slices before KCl addition. On the other hand, addition of 4-CIN induced larger [^{18}F]FDG uptake rates under the activated condition in comparison with the control condition. Because neurons cannot utilize lactate under the 4-CIN loaded conditions, this indicates that activated neurons consume lactate as an energy substrate. The lactate concentration in the incubation medium was increased with KCl treatment in both groups and the extent was slightly greater in 4-CIN group. These results suggested that: (1) the brain mainly uses glucose, not lactate, as an energy substrate in resting state; (2) when neuron is stimulated, excess amounts of lactate might be produced in astrocytes and the lactate is mobilized as an energy substrate.

Keywords: Lactate; Glucose; Rat brain slice; 2-Deoxy-2-[^{18}F]fluoro-D-glucose; Autoradiography; Cerebral energy metabolism

1. Introduction

The neuronal metabolic events that occur during functional activation are still partially unclear. Glucose has been thought as the only metabolic substrate of the brain for a long time (McIlwain and Bachelard, 1985). However, many researchers have recently been interested in lactate as an energy substrate in the brain, especially in neurons. Pellerin and Magistretti (1994) proposed an astrocyte–neuron lactate shuttle hypothesis (ANLSH), which claims the metabolic role of lactate in the brain. This model hypothesizes that neuronal activation stimulates the anaerobic production of lactate in neighbouring astrocytes. The produced lactate in astrocytes is then transferred to the neuron, which then uses the lactate as an energy substrate aerobically. In vivo studies have shown that the brain can consume lactate as a substrate (Ide and Secher, 2000; Smith et al., 2003). Magnetic resonance spectroscopy studies also show the increase of lactate production during cerebral activation (Frahm et al., 1997; Sappey-Marinier et al., 1992). Furthermore, in vitro studies have shown that lactate is utilized as an energy substrate in ischemic (Kitano et al., 2002) or hypoglycemic conditions (Izumi et al., 1997). On the other hand, Chih and Roberts (2003) support the conventional hypothesis that asserts that glucose is the primary substrate for both neurons and astrocytes during neural activated conditions. They claim that the experimental evidence of ANLSH is weak and that the existing evidence supports the conventional hypothesis. Therefore, the role of lactate in neuronal energy

* Corresponding author. Tel.: +81 53 435 2398; fax: +81 53 435 2398.
E-mail address: magata@hama-med.ac.jp (Y. Magata).

0168-0102/$ – see front matter
doi:10.1016/j.neures.2005.04.007

metabolism is not clearly elucidated, which has sparked interest in many researchers.

Recently, Tanaka et al. (2004) investigated the role of lactate in brain energy metabolism using the "bioradiography" system. "bioradiography" is the dynamic living brain slice imaging system for positron–emitter labeled compounds. They investigated the uptake of 2-deoxy-2-[^{18}F]fluoro-D-glucose ([^{18}F]FDG), which is a positron emitting radiotracer for glucose metabolism measurement, to rat brain slices. The slices were incubated in lactate or a monocarboxylate transporter (MCT) inhibitor, α-cyano-4-hydroxycinnamate (4-CIN), added Krebs–Ringer solution. [^{18}F]FDG uptake was decreased by the lactate application and increased by the 4-CIN application. These results suggested that lactate is used as an energy substrate in the brain in resting state. However, the contribution of lactate as an energy substrate during neural activated conditions has not been clarified.

Therefore, in this study, we investigated energy metabolism under neural activated conditions in the brain using the "bioradiography" system with [^{18}F]FDG and compared under resting state conditions.

2. Materials and methods

2.1. Materials

All chemicals used were reagent grade. α-Cyano-4-hydroxycinnamate (4-CIN) was purchased from Sigma (Milwaukee, WI, USA). Wistar rats were supplied by Japan SLC Co. Ltd. (Sizuoka, Japan). The present animal study was approved by the Animal Care and Use Committee of the Hamamatsu University School of Medicine.

2.2. Preparation of rat brain slices

After the decapitation of male Wistar rats (230–250 g), the brain was quickly removed and placed in an ice-cold oxygenated (95% O_2, 5% CO_2) Krebs–Ringer solution (124 mM NaCl, 5 mM KCl, 2 mM $CaCl_2$, 1 mM $MgCl_2$, 1.2 mM KH_2PO_4, 26 mM $NaHCO_3$, 5 mM glucose) for 3 min. Coronal slices (300 μm) were prepared using a microslicer (D.S.K. Super Microslicer, Dosaka EM, Kyoto, Japan) and transferred into the ice-cold Krebs–Ringer solution.

2.3. [^{18}F]FDG uptake study using the dynamic imaging system

[^{18}F]F^- was produced by a $^{18}O(p, n)^{18}F$ nuclear reaction using a Sumitomo CYPRIS HM18 cyclotron (Sumitomo Heavy Industries Ltd., Tokyo, Japan). Then [^{18}F]FDG was prepared from [^{18}F]F^- by the method of Hamacher et al. (1986) using an automated synthesis system (Cupid, Sumitomo Heavy Industries Ltd., Tokyo, Japan).

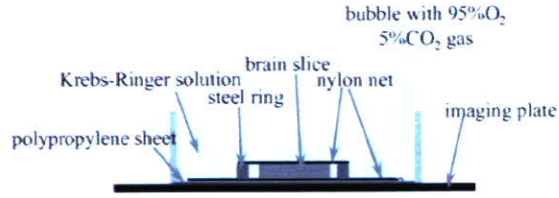

Fig. 1. Schematic side view of the incubation system for "bioradiography". Krebs–Ringer solution containing 1.5 MBq/mL of [^{18}F]FDG. Images were obtained in a dark environment at 35 °C.

The incubation was performed using the double polystyrene system as described by Murata et al. (1998). The system is described in Fig. 1. The Krebs–Ringer solution was filled into the outer chamber and the inner chamber was immersed in it. The bottom of the inner chamber was made with a nylon net and the bottom of the outer chamber was a 10 μm thick polyvinylidene chloride film that was penetrable to beta and gamma ray of ^{18}F. The prepared slices were placed in the inner chamber and were covered by a 300 μm stainless steel ring, as the upper side was braced by nylon net. After preincubation of the slices for 1 h at 35 °C, the inner chamber was taken out and immersed into another chamber that contained 1.5 MBq/mL of [^{18}F]FDG. The incubation volume was 100 mL for each chamber. During the incubation, Krebs–Ringer solution was bubbled with 95% O_2 and 5% CO_2 mixed gas. Ten brain slices were placed in each inner chamber.

For the 4-CIN added study, 4-CIN was added to the incubating solution and the pH was adjusted to 7.4 with NaOH (4-CIN added condition). The final concentration of 4-CIN was 0.5 mM. Control study was performed without 4-CIN (control condition). To take the images of the slices, the chamber was placed on the imaging plate (BAS-MS2040, Fuji Photo Film Co., Tokyo, Japan) and the plate was changed every 10 min. Then, the imaging plate was scanned with a computer-associated image analyzer (Fujix Bio-Imaging Analyzer, BAS-2000, Fuji Photo Film Co., Tokyo, Japan). To measure the background activity from the [^{18}F]FDG including solution over the brain slice, 300 μm nylon sheet was placed beside the brain slices. The incubation was carried out for 150 min. After 60 min incubation with [^{18}F]FDG, 50 mM of KCl with was added to each chamber. To adjust the osmolarity, KCl was dissolved in NaCl reduced Krebs–Ringer solution. For determination of lactate concentration of the incubation solution, 100 μL of the incubation solution was sampled every 20 min. The lactate concentration was then measured with an enzymatic bio-assay kit for L-lactate (R-Biopharm AG, Darmstadt, Germany).

2.4. Automatic registration of images

Sequential images from the imaging plate were automatically registered to the last image. To do this, each image was binarized by certain image threshold and then two-dimensional template matching technique was utilized for

the registration. Two circle regions of interest were placed on each brain region in each slice.

2.5. Analysis of [^{18}F]FDG uptake

[^{18}F]FDG uptake index, $Ci^*(t)/Cp^*(t)$ was calculated according to the method of Murata et al. (1999). $Ci^*(t)/Cp^*(t)$ can be represented as follows:

$$Ci^*(t)/Cp^*(t) = (ROI - NS)/(BG - NS)$$

where $Ci^*(t)$ is the radioactivity of a 300 μm thick brain slice at t, $Cp^*(t)$ the radioactivity of the 300 μm thick incubation medium, ROI the radioactivity signal on the imaging plate of region of interest in the brain slice (PSL: phosphostimulated luminescence/mm^2), NS the radioactivity on the imaging plate detected from the region beneath the 300 μm thick nylon sheet (PSL/mm^2), and BG is the radioactivity detected from bathing medium (PSL/mm^2). In our investigation, NS = 0.896 × BG. The [^{18}F]FDG uptake rate was determined from the slope of the time course of the [^{18}F]FDG uptake index curve.

2.6. Statistical analysis

Data are presented as the mean ± S.D. Statistical analysis was carried out using the Mann–Whitney U-test.

3. Results

3.1. Effect of 4-CIN on [^{18}F]FDG uptake

[^{18}F]FDG uptake increased with time in both 4-CIN added and control conditions. The results are summarized in Table 1. No significant difference was observed in the [^{18}F]FDG uptake rate between both conditions in all investigated brain regions before KCl addition. The uptake was accelerated by KCl addition but changes occurred at around 90 min, although KCl was added at 60 min (Fig. 2). Therefore, the [^{18}F]FDG uptake rate was determined using the plots from 0 to 60 min for resting state and those from 90 to 150 min for the KCl activated state. The increased extent of [^{18}F]FDG uptake rate by KCl addition was significantly larger for the 4-CIN added condition in the cortex, striatum, thalamus, and hippocampus. The autoradiograms of brain slices after KCl addition are shown in Fig. 3.

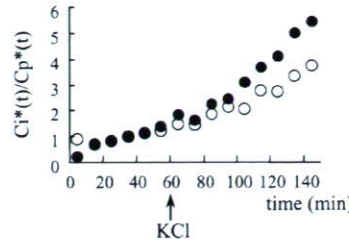

Fig. 2. Typical pattern of [^{18}F]FDG uptake index curve in the cortex in control (open circle) and 4-CIN added (filled circle) conditions. At 60 min after the start of incubation, 50 mM KCl was added to the solution. Values are means of two slices on a representative experiment.

3.2. Changes in lactate concentration in the [^{18}F]FDG incubation solution

Fig. 4 shows the changes in lactate concentration in the incubating solution. Before KCl addition, the lactate concentration was slightly increased with time in both 4-CIN added and control conditions. The lactate concentration was increased by KCl addition in both conditions. In contrast to the alteration of [^{18}F]FDG uptake after KCl addition, the increase of lactate concentration occurred just after the KCl addition. The extent of increase in lactate concentration was similar in both conditions.

4. Discussion

Glucose has been thought to be the only energy substrate of the brain. However, some investigators suggested that lactate can serve as an energy substrate in the brain both in vitro and in vivo. Magistretti et al. (1999) proposed the hypothesis that the activated neuron uses lactate and not glucose (ANLSH). Furthermore, they believed that lactate is produced in astrocytes then transferred to the neuron. To elucidate this hypothesis, we investigated the effect of the MCT inhibitor, 4-CIN.

Nine types of MCTs are known. It has been reported that the major glial MCT is MCT1. MCT2 or another isoform may be predominant on neurons (Debernardi et al., 2003;

Table 1
Effect of 4-CIN on [^{18}F]FDG uptake rate (min^{-1})

	Cortex	Striatum	Thalamus	Hippocampus
Before KCl				
Control	12.8 ± 4.2	18.9 ± 6.1	19.4 ± 5.3	14.9 ± 3.7
4-CIN	12.8 ± 4.2	23.8 ± 5.8	23.6 ± 8.6	18.3 ± 6.0
After KCl				
Control	40.3 ± 7.5 a	36.5 ± 14.5 b	29.6 ± 8.3 c	32.3 ± 7.9 d
4-CIN	75.1 ± 13.5 a	85.4 ± 18.7 b, f	82.5 ± 22.5 a, e	50.9 ± 10.9 c, g

The values are the slope (1000×) of [^{18}F]FDG uptake index curve of each study (Fig. 3). These were calculated by using linear regression analysis. Values are means ± S.D. of six to eight independent studies (12–16 slices). $P < 0.0001$ (a), $P < 0.001$ (b), $P < 0.01$ (c), $P < 0.05$ (d) compared with the corresponding before KCl value. $P < 0.001$ (e), $P < 0.01$ (f), $P < 0.05$ (g) compared with the corresponding control value.

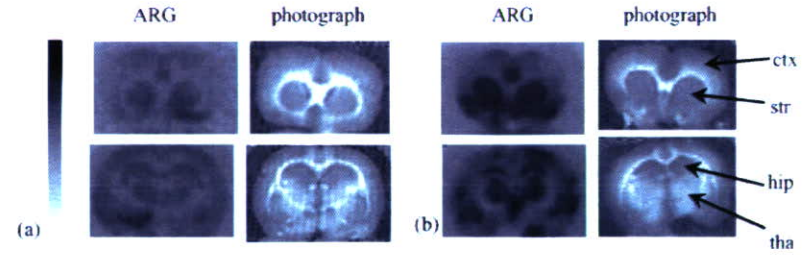

Fig. 3. Autoradiograms and photographs of coronally sectioned rat brain slices in control (a) and 4-CIN added (b) conditions. Images are obtained from 140 to 150 min after the start of incubation. ctx: Cerebral cortex; str: striatum; hip: hippocampus; tha: thalamus.

Halestrap and Price, 1999). Previous observations suggest that MCT2 is expressed in peripheral tissues, such as liver or heart, which mainly consume lactate. However, MCT1 is expressed in muscle, which preferentially releases lactate (Jackson and Halestrap, 1996). The K_m value for MCT1 is lower in pyruvate than lactate (Carpenter and Halestrap, 1994; Garcia et al., 1995). MCT2 displays the lowest K_m, which makes it particularly suitable for uptake of lactate. The observed distribution and K_m value of MCT1 and MCT2 would be consistent with the proposed concept of lactate exchange between astrocytes and neurons (Debernardi et al., 2003). Moreover, this concept is supported by the distribution of lactate dehydrogenase (LDH), which metabolizes lactate to pyruvate for aerobic glycolysis. LDH1 is the predominant LDH isoform found in neurons in adult brain and this isoform is predominantly expressed in peripheral tissues, which can oxidize lactate for energy production. In contrast, LDH5, which is found in tissues displaying anaerobic glycolysis, is expressed in astrocytes. 4-CIN blocked MCT2 about 20-fold more potently than MCT1 when the rat transporters were expressed in Xenopus oocytes (Broer et al., 1999). Cater et al. (2001) reported that 4-CIN does not act as the mitochondrial pyruvate transport blocker. On the other hand, McKenna et al. (2001) reported that 4-CIN affects lactate transport to mitochondria. In our investigation, no difference was seen in the lactate concentration in the incubation medium between the 4-CIN added condition and the control condition in resting state. This means mitochondrial aerobic metabolism was

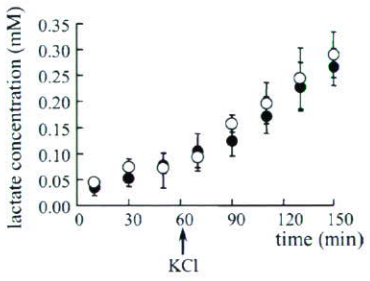

Fig. 4. Changes in lactate concentration of the incubating solution in control (open circle) and 4-CIN added (filled circle) conditions. At 60 min after the start of incubation, 50 mM KCl was added to the solution. Because lactate concentration was reduced after KCl addition, the concentration was corrected to that before KCl addition. Values are means and S.D. of six independent studies.

functional in both neurons and astrocytes. If 4-CIN has blocked the mitochondrial MCTs, glucose would not be metabolized aerobically through TCA cycle and lactate concentration would increase as a result. The added 4-CIN blocked lactate influx to the neuron from external solution through MCT2 and neurons could not use exogenous lactate as an energy substrate in the 4-CIN added condition.

The [^{18}F]FDG uptake rate was similar under both 4-CIN added and control conditions in all investigated brain regions before KCl addition. These observations suggest that neurons do not use exogenous lactate as a dominant energy substrate in resting state. Neurons and astrocytes take up glucose through the glucose transporter and utilize glucose as an energy substrate aerobically in each cell independently. However, Tanaka et al. (2004) have reported that 4-CIN causes increase of [^{18}F]FDG uptake in cerebral cortex but not in other brain regions by using the "bioradiography" system, although they did not show a good explanation for the regional differences (Tanaka et al., 2004). They added 4-CIN at 120 min from the beginning of the incubation with [^{18}F]FDG and gathered data for 360 min. The uptake rate increased from 120 min after the 4-CIN addition. We added 4-CIN from the beginning of the incubation and gathered data for 60 min before KCl addition. If we had followed longer, we might have had the same observation as Tanaka et al. (2004). Unfortunately, they did not check the lactate concentration in the incubation buffer. 4-CIN might affect mitochondrial MCTs or other systems in such long incubation times for rat brain slices in this system, although further investigation is needed.

High K^+ stimulation is different from physiological neuronal activation. However, high K^+ stimulates neurons by inducing depolarization and subsequent neurotransmitter release. It was earlier demonstrated that a high concentration of K^+ ions in the incubation solution enhances [^{14}C]deoxyglucose incorporation into brain slice preparations (Newman et al., 1988). Matsumura et al. (1995) also showed [^{18}F]FDG uptake enhancement to brain slices in high K^+ conditions. If neurons take up lactate and use it as an energy substrate under KCl stimulated conditions, 4-CIN causes energy deficiencies on neurons. Neurons will then take up glucose to satisfy the energy deficiency. In our study, KCl elevated the [^{18}F]FDG uptake rate in both 4-CIN added and control conditions, but the extent was significantly greater in the 4-CIN added group than in the control group. This result shows

that the neuron uses lactate preferably to glucose in stimulated states. However, lactate concentration in the incubation solution was increased to a similar extent in both groups even under the KCl stimulating condition. This might be explained if astrocytes released considerably large amounts of lactate for neuronal consumption although the consumed amount might have been small compared to the lactate amount in the incubating solution. Moreover, in our investigation, the increase in [^{18}F]FDG uptake was delayed about 30 min in both conditions. This means that the energy substrate demand occurs after some interval on KCl stimulation. The stored glycogen in astrocytes might be used as primary before exogenous glucose, although we do not have any evidence. These phenomena are of our interest to explore the cerebral energy regulation system.

These results suggested that: (1) the brain mainly uses glucose, not lactate, as an energy substrate in resting state; (2) when the neuron is stimulated, excess amounts of lactate are produced in astrocytes and the lactate is mobilized as an energy substrate for neurons. The ANLSH is partly supported by our investigation. However, our study cannot claim that stimulated neurons use "only" lactate and not glucose. This should be investigated further hereafter.

Acknowledgements

This study was supported by Grants-in-Aid for General Scientific Research (No. 14770486) from the Ministry of Education, Culture, Sports, Science and Technology of Japan. A part of this study was also supported by Grant in Aide for the Center of Excellence (COE) at Hamamatsu University School of Medicine "Medical Photonics" from the Ministry of Education, Culture, Sports, Science and Technology of Japan, by the Program for Promotion of Fundamental Studies in Health Science of the Organization for Pharmaceutical Safety and by Mitsubishi Pharma Research Foundation. The authors thank Mr. N. Ejima, Institute for Biofunctional Research Ltd. for the cyclotron operation and [^{18}F]FDG synthesis, and Dr. Y. Kiyono, Kyoto University for technical assistance and useful discussion.

References

Broer, S., Broer, A., Schneider, H.P., Stegen, C., Halestrap, A.P., Deitmer, J.W., 1999. Characterization of the high-affinity monocarboxylate transporter MCT2 in *Xenopus laevis* oocytes. Biochem. J. 341, 529–535.

Carpenter, L., Halestrap, A.P., 1994. The kinetics, substrate and inhibitor specificity of the lactate transporter of Ehrlich–Lettre tumour cells studied with the intracellular pH indicator BCECF. Biochem. J. 304, 751–760.

Cater, H.L., Benham, C.D., Sundstrom, L.E., 2001. Neuroprotective role of monocarboxylate transport during glucose deprivation in slice cultures of rat hippocampus. J. Physiol. 531, 459–466.

Chih, C.P., Roberts Jr., E.L., 2003. Energy substrates for neurons during neural activity: a critical review of the astrocyte-neuron lactate shuttle hypothesis. J. Cereb. Blood Flow Metab. 23, 1263–1281.

Debernardi, R., Pierre, K., Lengacher, S., Magistretti, P.J., Pellerin, L., 2003. Cell-specific expression pattern of monocarboxylate transporters in astrocytes and neurons observed in different mouse brain cortical cell cultures. J. Neurosci. Res. 73, 141–155.

Frahm, J., Krueger, G., Merboldt, K.D., Kleinschmidt, A., 1997. Dynamic NMR studies of perfusion and oxidative metabolism during focal brain activation. Adv. Exp. Med. Biol. 413, 195–203.

Garcia, C.K., Brown, M.S., Pathak, R.K., Goldstein, J.L., 1995. cDNA cloning of MCT2, a second monocarboxylate transporter expressed in different cells than MCT1. J. Biol. Chem. 270, 1843–1849.

Halestrap, A.P., Price, N.T., 1999. The proton-linked monocarboxylate transporter (MCT) family: structure, function and regulation. Biochem. J. 343, 281–299.

Hamacher, K., Coenen, H.H., Stocklin, G., 1986. Efficient stereospecific synthesis of no-carrier-added 2-[^{18}F]-fluoro-2-deoxy-D-glucose using aminopolyether supported nucleophilic substitution. J. Nucl. Med. 27, 235–238.

Ide, K., Secher, N.H., 2000. Cerebral blood flow and metabolism during exercise. Prog. Neurobiol. 61, 397–414.

Izumi, Y., Katsuki, H., Zorumski, C.F., 1997. Monocarboxylates (pyruvate and lactate) as alternative energy substrates for the induction of long-term potentiation in rat hippocampal slices. Neurosci. Lett. 232, 17–20.

Jackson, V.N., Halestrap, A.P., 1996. The kinetics, substrate, and inhibitor specificity of the monocarboxylate (lactate) transporter of rat liver cells determined using the fluorescent intracellular pH indicator, 2′,7′-bis(-carboxyethyl)-5(6)-carboxyfluorescein. J. Biol. Chem. 271, 861–868.

Kitano, T., Nisimaru, N., Shibata, E., Iwasaka, H., Noguchi, T., Yamada, K., 2002. Lactate utilization as an energy substrate in ischemic preconditioned rat brain slices. Life Sci. 72, 557–564.

Magistretti, P.J., Pellerin, L., Rothman, D.L., Shulman, R.G., 1999. Energy on demand. Science 283, 496–497.

Matsumura, K., Bergstrom, M., Onoe, H., Takechi, H., Westerberg, G., Antoni, G., Bjurling, P., Jacobson, G.B., Langstrom, B., Watanabe, Y., 1995. In vitro positron emission tomography (PET): use of positron emission tracers in functional imaging in living brain slices. Neurosci. Res. 22, 219–229.

McIlwain, H., Bachelard, H.S., 1985. Biochemistry and the Central Nervous System, fifth ed. Churchill Livingstone, New York.

McKenna, M.C., Hopkins, I.B., Carey, A., 2001. Alpha-cyano-4-hydroxycinnamate decreases both glucose and lactate metabolism in neurons and astrocytes: implications for lactate as an energy substrate for neurons. J. Neurosci. Res. 66, 747–754.

Murata, T., Omata, N., Fujibayashi, Y., Waki, A., Sadato, N., Yoshimoto, M., Omori, M., Isaki, K., Yonekura, Y., 1999. Dynamic changes in glucose metabolism induced by thiamine deficiency and its replenishment as revealed by a positron autoradiography technique using rat living brain slices. J. Neurol. Sci. 164, 29–36.

Murata, T., Waki, A., Omata, N., Fujibayashi, Y., Sadato, N., Yano, R., Yoshimoto, M., Isaki, K., Yonekura, Y., 1998. Dynamic changes in glucose metabolism by lactate loading as revealed by a positron autoradiography technique using rat living brain slices. Neurosci. Lett. 249, 155–158.

Newman, G.C., Hospod, F.E., Patlak, C.S., 1988. Brain slice glucose utilization. J. Neurochem. 51, 1783–1796.

Pellerin, L., Magistretti, P.J., 1994. Glutamate uptake into astrocytes stimulates aerobic glycolysis: a mechanism coupling neuronal activity to glucose utilization. Proc. Natl. Acad. Sci. U.S.A. 91, 10625–10629.

Sappey-Marinier, D., Calabrese, G., Fein, G., Hugg, J.W., Biggins, C., Weiner, M.W., 1992. Effect of photic stimulation on human visual cortex lactate and phosphates using 1H and 31P magnetic resonance spectroscopy.

Smith, D., Pernet, A., Hallett, W.A., Bingham, E., Marsden, P.K., Amiel, S.A., 2003. Lactate: a preferred fuel for human brain metabolism in vivo. J. Cereb. Blood Flow Metab. 23, 658–664.

Tanaka, M., Nakamura, F., Mizokawa, S., Matsumura, A., Matsumura, K., Murata, T., Shigematsu, M., Kageyama, K., Ochi, H., Watanabe, Y., 2004. Role of lactate in the brain energy metabolism: revealed by bioradiography. Neurosci. Res. 48, 13–20.

ORIGINAL ARTICLE

Annals of Nuclear Medicine Vol. 19, No. 6, 425–433, 2005

Use of reference tissue models for quantification of histamine H_1 receptors in human brain by using positron emission tomography and [^{11}C]doxepin

Atsuro SUZUKI,* Manabu TASHIRO,** Yuichi KIMURA,*** Hideki MOCHIZUKI,**** Kenji ISHII,*** Hiroshi WATABE,***** Kazuhiko YANAI,**** Kiichi ISHIWATA*** and Keizo ISHII*

*Department of Quantum Science and Energy Engineering, Tohoku University
**Cyclotron and Radioisotope Center, Tohoku University
***Positron Medical Center, Tokyo Metropolitan Institute of Gerontology
****Department of Pharmacology, Tohoku University School of Medicine
*****Department of Investigative Radiology, Research Institute, National Cardiovascular Center

The aim of the present study is to evaluate the validity of the simplified reference tissue model (SRTM) and of Logan graphical analysis with reference tissue (LGAR) for quantification of histamine H_1 receptors (H1Rs) by using positron emission tomography (PET) with [^{11}C]doxepin. These model-based analytic methods (SRTM and LGAR) are compared to Logan graphical analysis (LGA) and to the one-tissue model (1TM), using complete datasets obtained from 5 healthy volunteers. Since H1R concentration in the cerebellum can be regarded as negligibly small, the cerebellum was selected as the reference tissue in the present study. The comparison of binding potential (*BP*) values estimated by LGAR and 1TM showed good agreement; on the other hand, SRTM turned out to be unstable concerning parameter estimation in several regions of the brain. By including the results of noise analysis, LGAR became a reliable method for parameter estimation of [^{11}C]doxepin data in the cortical regions.

Key words: model-based analysis, histamine H_1 receptor, [^{11}C]doxepin, PET

INTRODUCTION

THE HISTAMINERGIC NEURON SYSTEM in the brain plays important roles in various physiological functions such as wakefulness, cognition and memory.[1–3] These brain functions are mediated mainly by histamine H_1 receptors (H1Rs), one of 4 known subtypes (H_1, H_2, H_3, and H_4).[1] For mapping the distribution of H1Rs in the human brain, positron emission tomography (PET) has been used with [^{11}C]-labeled doxepin, a potent H1R antagonist.[4] [^{11}C]doxepin is radiotracer of choice because of its high affinity to H1Rs and its ability to penetrate the blood-brain barrier.[5] PET with [^{11}C]doxepin has been applied to the investigation of various pathological states including Alzheimer's disease and epilepsy,[6,7] as well as sedation due to antihistamines observed in patients with various disorders.[2,8–10]

In most H1R mapping studies, the binding potential (*BP*) of [^{11}C]doxepin to H1Rs is calculated using the graphical method introduced by Logan and colleages.[11] As part of our recent efforts to establish a suitable analytical method for [^{11}C]doxepin, we first demonstrated that the one-tissue model (1TM) was more stable in parameter estimation of [^{11}C]doxepin kinetics than the two-tissue model (2TM) which leads to a large variation in parameter values, depending strongly upon the startup parameters.[12] Thereafter, we also developed a short (15-min-long) static scan protocol of one-point blood sampling to reduce physical and psychological stress of test persons in clinical trials, in which the persons are to be scanned 3 to 4 times.[13] So far, we have not examined the possible application of reference tissue models to [^{11}C]doxepin data, where blood sampling is not needed. Two major reference tissue models are available: the simplified reference tissue model (SRTM)[14] and Logan graphical analysis with

Received November 15, 2004, revision accepted March 16, 2005.

For reprint contact: Keizo Ishii, D.Sci., Department of Quantum Science and Energy Engineering, Tohoku University, Aramaki-aza-aoba 01, Aoba-ku, Sendai 980–8579, JAPAN.
E-mail: keizo.ishii@qse.tohoku.ac.jp

reference tissue (LGAR).[15]

A compartment model for receptor analysis should be developed based on the kinetic tracer behavior in target organs. Usually, this behavior is described with a three-compartment model (two-tissue model: 2TM),[16] but if rapid equilibrium occurs among free, nonspecifically and specifically bound compartments, a 1TM is suitable for the kinetic analysis.[17] In fact, our previous study already demonstrated that 1TM was suitable for describing the kinetic data of [^{11}C]doxepin whereas the results based on 2TM highly depended on initial parameter estimation so that different initial values produced different results.[12] Therefore, 2TM was excluded from the present evaluation. In the present study, H1R-[^{11}C]doxepin binding parameters estimated by 2 reference tissue models, SRTM and LGAR, were compared to those calculated by LGA and by 1TM. Reliability of these analytical methods was also examined by comparing the obtained parameters to those calculated by 1TM, probably the most reliable method in the present evaluation.

MATERIALS AND METHODS

Subjects

Five healthy male volunteers, 21–27 years old, participated in the present study. None had any previous history of psychiatric or neurological disorders and none of them showed anatomical abnormalities in brain MRI images. Written informed consent was obtained from every subject before enrollment in the present study. The volunteers were asked to abstain from taking medication for a week before the study, and from taking tobacco, alcohol and caffeine on the day of experiment. The study was approved by the respective ethics committees of the Tokyo Metropolitan Institute of Gerontology and of Tohoku University Graduate School of Medicine, and was performed in compliance with relevant laws.

PET measurement

Dynamic scans in two-dimensional mode were performed using Headtome-V (Shimadzu Co., Kyoto, Japan) with 63 slices of 128-by-128 voxels each at transverse resolution of 4.5 mm full width of half maximum (FWHM) and at axial resolution of 5.8 mm FWHM. PET images were reconstructed with a filtered backprojection algorithm, and corrections were applied for dead time, detector uniformity and photon attenuation. The frame arrangement was 10 sec × 6 frames, 30 sec × 3 frames, 60 sec × 5 frames, 2.5 min × 5 frames and 5 min × 14 frames for a total of 90 minutes and [^{11}C]doxepin was prepared as previously described.[12] The injected radioactivity dose of [^{11}C]doxepin was 493 ± 109 MBq and the cold mass was 23 ± 16 nmol (mean ± SD). Arterial blood was sampled every 10 sec for the first 150 sec post-injection and afterwards at 3, 5, 7, 10, 15, 20, 30, 40, 50, 60, 75 and 90 min. Metabolite analysis was carried out using 6 plasma samples obtained 3, 10, 20, 30, 40 and 60 min after the injection as previously described.[12]

Model-based analysis

The 2TM provides a general framework for model-based analysis that consists of a plasma compartment (C_p) and two-tissue compartments: one compartment is for the free and nonspecifically bound ligands (C_{f+ns}), and the other is for the specifically bound ligands (C_s). The transfer of the ligand across compartments is governed by 4 fractional rate constants, K_1, k_2, k_3 and k_4, where K_1 is the influx rate constant into C_{f+ns}, k_2 is the efflux rate constant from C_{f+ns}, k_3 is the association rate constant into C_s, and k_4 is the dissociation rate constant from C_s, respectively. If the association and dissociation rates between free ligands and receptors are sufficiently rapid compared to the transport parameters K_1 and k_2, the model can be simplified using a one-tissue compartment, where all of the free ligands and nonspecifically and specifically bound ligands are represented by a single tissue compartment. This model is the 1TM,[17] where the concentration time function $C_T(t)$ in a certain regional tissue is expressed as follows,

$$C_T(t) = K_1 C_P(t) \otimes e^{-k_{2a}t} \quad (1)$$

where $C_P(t)$ is the concentration time function in the plasma, and k_{2a} is the efflux rate constant from the single tissue compartment. The distribution volume (DV) can be written as $DV = K_1/k_{2a} = K_1/k_2\,(1 + k_3/k_4)$. Provided that the H1R concentration in the reference tissue is negligibly small and that K_1/k_2 is constant in the all brain regions, the binding potential ($BP = k_3/k_4$) can be obtained as $BP = DV/DV^{REF} - 1$, where DV^{REF} is DV in the reference tissue. In the present study, the cerebellum was used as the reference tissue because of the negligibly small H1R concentration in this region.

In SRTM,[14] the target and reference tissues are described as a one-tissue model. If K_1/k_2 is constant in the all brain regions, $C_T(t)$ in the tissue is expressed as follows,

$$C_T(t) = R_1 C_R(t) + \left\{ k_2 - \frac{R_1 k_2}{1 + k_3/k_4} \right\} C_R(t) \otimes e^{-k_2/(1+k_3/k_4)t} \quad (2)$$

where $C_R(t)$ is the concentration time function in the reference region, and R_1 is the ratio of delivery to the regional tissue compared to the reference region (ratio of influx). This method can avoid the complexity of arterial blood sampling.

The formula for LGA is expressed as follows:[11]

$$\frac{\int_0^T C_T(t)dt}{C_T(T)} = DV \frac{\int_0^T C_P(t)dt}{C_T(T)} + a_1 \quad (3)$$

where the values of the slope DV and the intercept a_1 are obtained by linear regression. The BP value is obtained as $BP = DV/DV^{REF} - 1$. LGAR[15] is expressed as follows:

$$\frac{\int_0^T C_T(t)dt}{C_T(T)} = DVR\left(\frac{\int_0^T C_R(t)dt + C_R(t)/k_2'}{C_T(T)}\right) + a_2 \quad (4)$$

where DVR is the distribution volume ratio (DV/DV^{REF}), a_2 is an intercept term, and k_2' is an average value in the reference tissue. Then BP is obtained as $BP = DVR - 1$, and the complexity of arterial blood sampling is avoided.

Data analysis

Regions of interest (ROIs) were drawn on 5 cortical structures (the frontal, temporal, occipital, parietal and cingulate cortices) bilaterally, 3 subcortical structures (the thalamus, caudate nucleus and putamen) bilaterally, and on the midbrain centrally. Two ROIs in right and left regions were drawn on cortical and subcortical structures. In results, 17 ROI data were obtained to obtain averaged tissue time-activity curves (tTACs) as reported previously.[12] One additional ROI was drawn on the cerebellum to obtain an averaged tTAC in the reference tissue.

In 1TM and SRTM analysis, parameters were estimated in standard nonlinear fitting algorithms of the Gauss-Newton type. The nonlinear regression was considered to have converged if all parameters had been changed by less than 0.1% from the previous iteration. Failure of convergence was declared if nonlinear regression failed to reach convergence after 100 iterations, and if the determinant of the normal equation's coefficient matrix was less than 10^{-20}. The initial values of K_1 and k_2 in 1TM were 0.5 [ml/g/min] and 0.02 [/min], respectively, and those of R_1, k_2 and BP in SRTM were 1, 0.01 [/min] and 0.5, respectively. Delay between tTAC and the plasma time-activity curve (pTAC) was estimated using an averaged tTAC of the whole-brain. In the present study, cerebral blood volume was disregarded because it is generally small (3–5%).[18]

BP values derived from different methods were compared in terms of the following criteria: 1) failure rate, 2) physiological rationality, and 3) sensitivity to noise.

1) Failure rate

In general, a failure in parameter estimation occurs in the following cases: a) when the nonlinear regression procedure fails to reach convergence, b) when the estimated parameter is unstable against variation of the initial parameter values in nonlinear regression, c) when BP values calculated by $DVR - 1$ become negative, d) when the standard error in the estimated parameter becomes very large. Note that the standard error here means the error in a parameter caused by the inherent uncertainty of this estimation procedure. The standard error of the parameter was obtained from the diagonal of the covariance matrix, and the result of parameter estimation was defined as "failure" when the standard error exceeded 30%.[19] In the present analysis, a total of 85 ROIs (17 ROIs from each of 5 subjects) were examined. Then, the failure rate of each modeling procedure was expressed as [number of regions whose estimation failed]/85 × 100%.

2) Physiological rationality

Physiological rationality was assessed by comparing the estimated BP values to H1R densities measured in the brain *in vitro* using [^{3}H]doxepin, as reported by Kanba and Richelson.[20] In addition, correlations were examined between BP values calculated by 1TM and those by the other methods using Pearson's correlation test.

3) Sensitivity to noise

Simulation was performed to evaluate the sensitivity to noise for each model-based method. This evaluation was carried out for BP estimation for the temporal cortex that was rich in H1Rs and in the occipital cortex that was relatively poor in H1Rs, by using the cerebellum as the reference region. Simulation data (ROI_N) are expressed as the following:

$$ROI_N(t) = ROI(t) + SD(t) \times N(0,1) \quad (5)$$

$$SD(t) = \sqrt{\frac{c \times ROI(t) \times e^{\lambda t}}{\Delta t}}$$

where a non-dimensional constant c determines the noise level, λ is a decay constant of the isotope, Δt is frame length, $N(0,1)$ is a pseudo-random number of a Gauss distribution with zero mean and standard deviation of one.[21]

In the present simulation, random noise was introduced and noisy datasets were analyzed with SRTM, LGAR, LGA and 1TM, at 8 different noise levels (noise level c = 5, 10, 15, 20, 25, 30, 35, 40). The noise levels of the actual brain image data were considered to remain within the range of the noise levels mentioned above. In the present simulation analysis, 1000 different curves were generated for each noise level, and the effects of noise levels on the results were evaluated using a bias, i.e. the difference between the true BP values and BP values obtained in 1000 simulations, for each modeling method.

Simulation on the effect of nonspecific binding

In order to investigate the effect of nonspecific binding on the parameter estimation, another simulation was performed according to the following procedure. Simulated tTACs in the various cortical regions and the reference tissue (the cerebellum) were generated by 1TM with varying nonspecific binding values of DV^{REF} = 5, 10, 15, 20, 25, 30. Based on an assumption that nonspecific binding is equal in the target and reference regions, DV^{REF} was set to be identical to the nonspecific binding in the target regions in this simulation analysis. Based on the results of ROI analysis in the temporal cortex, the parameters K_1 and DV^{ROI} in the ROI were fixed at 0.495 [ml/g/min] and 36.5, respectively where DV^{ROI} represented the